

The TeV Cosmic Ray Bump: a Message from Epsilon Indi or Epsilon Eridani Star?

MIKHAIL A. MALKOV¹ AND IGOR V. MOSKALENKO²

¹*Department of Physics and CASS, University of California San Diego, La Jolla, CA, 92093, USA*

²*Hansen Experimental Physics Laboratory and Kavli Institute for Particle Astrophysics and Cosmology, Stanford University, Stanford, CA 94305, USA*

ABSTRACT

A recently observed bump in the cosmic ray (CR) spectrum from 0.3–30 TV is likely caused by a stellar bow shock that reaccelerates *preexisting* CRs, which further propagate to the Sun along the magnetic field lines. Along their way, these particles generate an Iroshnikov-Kraichnan (I-K) turbulence that controls their propagation and sustains the bump. *Ad hoc* fitting of the bump shape requires six adjustable parameters. Our model requires none, merely depending on *three physical unknowns that we constrain using the fit*. These are the shock Mach number, M , its size, l_{\perp} , and the distance to it, ζ_{obs} . Altogether, they define the bump rigidity R_0 . With $M \approx 1.5$ – 1.6 and $R_0 \approx 4.4$ TV, the model fits the data with $\approx 0.08\%$ accuracy. The fit critically requires the I-K spectrum predicted by the model and rules out the alternatives. These fit’s attributes make an accidental agreement highly unlikely. In turn, R_0 and M derived from the fit impose the distance-size relation on the shock: $\zeta_{\text{obs}}(\text{pc}) \sim 10^2 \sqrt{l_{\perp}(\text{pc})}$. For sufficiently large bow shocks, $l_{\perp} = 10^{-3}$ – 10^{-2} pc, we find the distance of $\zeta_{\text{obs}} = 3$ – 10 pc. Three promising stars in this range are: the Scholz’s Star at 6.8 pc, Epsilon Indi at 3.6 pc, and Epsilon Eridani at 3.2 pc. Based on their current positions and velocities, we propose that Epsilon Indi and Epsilon Eridani can produce the observed spectral bump. Moreover, Epsilon Eridani’s position is only $\sim 6.7^\circ$ off of the magnetic field direction in the solar neighborhood, which also changes the CR arrival direction distribution. Given the proximity of these stars, the bump appearance may change in a relatively short time.

Keywords: cosmic rays — diffusion — ISM: general

1. INTRODUCTION

Cosmic ray (CR) observations have much improved over the past decade and encouraged a deep rethinking of ways in which CRs are accelerated and transported. New features, such as breaks and significant differences in the spectral indices of different species, are being discovered in the energy range that deemed as well-studied (ATIC-2 – Panov et al. 2009, CREAM – Ahn et al. 2010; Yoon et al. 2011, PAMELA – Adriani et al. 2011, Fermi-LAT – Ackermann et al. 2014, AMS-02 – Aguilar et al. 2015a,b, 2017, 2018a,b; Aguilar et al. 2020, NUCLEON – Atkin et al. 2018, 2019; Grebenyuk et al. 2019a,b, CALET – Adriani et al. 2019, DAMPE – An et al. 2019). These features bear the signatures of CR acceleration processes and their propagation history.

A flattening in the spectra of CR p and He at ~ 300 GV was discovered first (Ahn et al. 2006, 2010; Adriani et al. 2011) giving raise to a number of different interpretations. With new accurate measurements of spectra of several primary (p , He, C, O, Ne, Mg, Si) and secondary (Li, Be, B) species becoming available from AMS-02 (Aguilar et al. 2015a,b, 2017, 2018a,b; Aguilar et al. 2020), only two main interpretations remain. These are (i) the intrinsic spectral breaks in the injection spectra of typical CR sources or two different types of sources with soft and hard spectra (a so-called “injection scenario,” Vladimirov et al. 2012), and (ii) a break in the spectrum of interstellar turbulence resulting in the break in the diffusion coefficient (a so-called “propagation sce-

nario,” Vladimirov et al. 2012; Blasi et al. 2012; Aloisio et al. 2015). The latter has very few free parameters and predicts that the spectral index change before/after the break in the spectra of secondary species $\Delta\gamma_{\text{sec}}$ should be twice as large as the spectral index change in the spectra of primary species $\Delta\gamma_{\text{sec}} \approx 2\Delta\gamma_{\text{pri}}$. This scenario seems to be well-supported by the AMS-02 data (see fits and a discussion in Boschini et al. 2020a,b).

Another spectral feature, a softening in the spectrum of protons and He at ~ 10 – 30 TV, was also found and seems to be well established now (Ahn et al. 2006; Atkin et al. 2018, 2019; Grebenyuk et al. 2019a; Adriani et al. 2019; An et al. 2019, see also parameterizations in Boschini et al. 2020b). Even though the two mentioned scenarios work well for one break, it is hard to imagine that the injection spectrum of an ensemble of CR sources and/or the spectrum of interstellar turbulence conspire to produce two relatively sharp breaks one decade in rigidity apart on a large Galactic scale. More likely explanation is the presence of a local CR source, where both breaks would form by a fresh primary component with a harder spectrum and an appropriate cutoff produced by the local source. Meanwhile, a scenario with a local supernova (SN) explosion (e.g., Fang et al. 2020; Fornieri et al. 2020; Yuan et al. 2020) predicts no breaks in the *secondary* component (Vladimirov et al. 2012) and thus is unfeasible. Moreover, the unprecedented accuracy with which the sharp break in the spectrum is measured rules out a linear composition

of independent sources. The transition would be too smooth unless the sources conspire to replace each other at the transition point (Niu 2020).

The fact that the spectra of secondaries are also flattening above the first break similar to the primaries, albeit with different spectral index, implies that the secondary species have already been present in the CR mixture that the bump is made of. *Therefore, the bump has to be made out of the preexisting CRs with all their primaries and secondaries that have spent millions of years in the Galaxy.* There are two possibilities: either the bump was being formed in a significant part of the Galaxy simultaneously with the secondaries over the CR confinement time, or it has been created locally, relatively short time before we started observing it. We will argue that the second possibility is more likely.

Worth mentioning is the sharpness of the bump that may provide useful restrictions on the distance to its formation site. Originating in remote objects would result in a smoother appearance due to the diffusive propagation and mixing with old CRs. An estimate of the maximum distance, provided in Sect. 4, limits it to a 3–10 pc, thus suggesting a field-aligned CR propagation from the bump formation site directly to the observer. Assuming, still, that most of the CR accelerators collectively produce a featureless power-law spectrum, in this paper we are proposing a bow shock of a passing star and/or a magnetosonic shock in the Local Bubble as a possible origin of the feature recently observed in the sub-TeV–10 TeV energy range.

We build a relevant CR reacceleration-propagation model and argue that it reproduces the data not coincidentally because:

- This model provides a fit to a complex high-fidelity spectrum that contains two consecutive breaks with only a 0.08% deviation over nearly four decades in energy with no adjustable parameters (other than the distance, size, and Mach number of the shock);
- The fit critically requires specific wave turbulence, *self-driven by reaccelerated CR*, shown to be of an Iroshnikov-Kraichnan (I-K) type. Other turbulence spectra, such as the more common for the background interstellar medium Kolmogorov spectrum, do not fit the data;
- There exists at least one suitable shock that is magnetically connected with the Sun well within the uncertainties of the local magnetic field direction, it is a very powerful termination shock around Epsilon Eridani star at 3.2 pc; it is different from the bow shock, but may also reaccelerate CRs.

The remainder of the paper is organized as follows. In Sect. 2 we assess the local ISM environment for shocks suitable to our model. In Sect. 3 we consider a modification of the preexisting CR spectrum by such a shock. Sect. 4 describes the propagation of the modified CR spectrum to the observer through a self-driven turbulence. In Sect. 5 we determine the unknown physical parameters of the shock by

fitting the data to our model. In Sect. 6 we discuss possible shock candidates around passing stars. In Sect. 7 we evaluate the CR anisotropy associated with the nearby shock. In Sect. 8 we describe the topology of the local magnetic field and discuss its perturbation mechanisms. We conclude with a brief summary in Sect. 9 and a discussion in Sect. 10. Appendices A and B describe the formalism of the generation of turbulence by the reaccelerated particles and the wave energy transformation. Appendix C details an estimate of the distance to the hypothetical bow-shock. Appendix D supplements the discussion of the large- and small-scale anisotropy provided in Sect. 7.

2. THE LOCAL BUBBLE

The Local Bubble is a low density region of the size of ~ 200 pc around the Sun filled with hot H I gas that was formed in a series of SN explosions (e.g., Sfeir et al. 1999; Frisch et al. 2011). Studies suggest 14–20 SN within a moving group, whose surviving members are now in the Scorpius-Centaurus stellar association (Frisch et al. 2011; Breitschwerdt et al. 2016).

An excess of radioactive ^{60}Fe found in deep ocean core samples of FeMn crust (Knie et al. 1999, 2004; Wallner et al. 2016), in the Pacific Ocean sediments (Ludwig et al. 2016), in lunar regolith samples (Cook et al. 2009; Fimiani et al. 2012, 2014), and more recently in the Antarctic snow (Koll et al. 2019) indicates that it may be deposited by SN explosions in the solar neighborhood. Observation of ^{60}Fe (the half-life $\tau_{1/2} \sim 2.6$ Myr, Rugel et al. 2009) in CRs by ACE-CRIS spacecraft (Binns et al. 2016), while only an upper limit for ^{59}Ni ($\tau_{1/2} \sim 76$ kyr) is established (Wiedenbeck et al. 1999), suggests $\gtrsim 100$ kyr time delay between the ejecta and the next SN, and thus SN events should be clustered in space and time. A newly found excess at 1–2 GV in the spectrum of CR iron (Boschini et al. 2021) derived from the combined Voyager 1 (Cummings et al. 2016), ACE-CRIS, and AMS-02 (Aguilar et al. 2021) data supports this picture.

Currently, there is no general agreement on the exact number of SNe events and their precise timing, but it is clear that there could have been several events during the last ~ 10 Myr at distances of up to 100 pc (Wallner et al. 2016). The most recent SN events in the solar neighborhood were 1.5–3.2 Myr and 6.5–8.7 Myr ago (Fry et al. 2015; Wallner et al. 2016). The measured spread of the signal is ~ 1.5 Myr (Fry et al. 2015). However, each of these events could, in principle, consist of several consequent SN explosions separated by some 100 kyr, as an estimated time spread for a single SN, located at ~ 100 pc from the Earth, is just ~ 100 –400 kyr and the travel time is ~ 200 kyr. A detailed modeling by Breitschwerdt et al. (2016) indicates two SNe at distances 90–100 pc with the closest occurred 2.3 Myr ago at present-day Galactic coordinates $(l, b) = (327^\circ, 11^\circ)$, and the second-closest exploded about 1.5 Myr ago at $(343^\circ, 25^\circ)$, both with stellar masses of $\sim 9M_\odot$.

The consequent SN events generated multiple shocks that are likely still present in the Local Bubble. The typical lifetime of such shocks ~ 2 Myr can be estimated assuming that

the shock speed is equal to the speed of sound in a 10^6 K plasma and a distance of 200 pc (Berghöfer & Breitschwerdt 2002). The same ballpark estimate can be obtained, if one assumes the old shock velocity of $\sim 100 \text{ km s}^{-1}$ – comparable to the typical velocity of the random motions in the interstellar medium (ISM). The shock could have also emerged more recently from a decaying turbulence left behind after the last SN events by wave steepening and shock coalescence.

In fact, radio observations and sometimes X- and γ -rays reveal structures, often referred to as “radio loops,” that cover a considerable area of the sky. There are at least 17 known structures (for details, see Vidal et al. 2015, and references therein) with the radii of tens of degrees that can be as large as $\sim 80^\circ$. The best-known is Loop I, which has a prominent part of its shell aligned with the North Polar Spur. The spectral indices of these structures indicate a nonthermal (synchrotron) origin for the radio emission, but the origin of the loops themselves remains unclear. One of the major limitations is the lack of precise measurements of their distances. However, it is clear that some of them could be the old SNRs and their huge angular sizes hint at their proximity to the solar system.

That was the original motivation for the present paper. However, in the process of writing an interesting alternative emerged: *a bow shock of a star rapidly moving in the solar neighborhood*. Such bow shocks are abundant in the Galaxy as clearly seen in images¹ by the Hubble Space Telescope, and are able to reaccelerate CRs. We discuss such a possibility in Sect. 6. A subset of fast moving stars is likely to be produced by the outer Lindblad resonant scattering (Dehnen 1999). The formalism described in the following sections is equally suitable for both scenarios, a magnetosonic shock and/or a passing star.

3. SPECTRUM MODIFICATION BY A WEAK SHOCK

Given the requirements for the observed sharp breaks in the CR spectrum, we approach the problem of their origin as follows. Consider a weak, planar magnetosonic shock propagating through the rarefied plasma in the Local Bubble. Assume the shock is moving at a speed u_1 in the positive x -direction, with which the ambient magnetic field makes an angle ϑ_{nB} . At first, we will describe the CR distribution both upstream and downstream of the shock by a stationary, convection-diffusion equation in one dimension. In obtaining its solution and analyzing whether it has a potential to reproduce the observed bump at some distance upstream, we will follow the CRs reaccelerated at the shock as they propagate along the magnetic flux tube, whose foot is on the shock surface. The propagation problem is two-dimensional, at a minimum, and we will address it in Sect. 4, including its connection to the one-dimensional reacceleration problem we consider in this section.

The convection-diffusion equation for the particle distribution function f near the shock reads

$$u \frac{\partial f}{\partial x} - \frac{\partial}{\partial x} \kappa \frac{\partial f}{\partial x} = \frac{1}{3} \frac{du}{dx} p \frac{\partial f}{\partial p}. \quad (1)$$

Here p is the particle momentum and the flow velocity has the following values, respectively ahead and behind of the shock,

$$u(x) = \begin{cases} -u_1, & x \geq 0, \\ -u_2, & x < 0, \end{cases} \quad u_1 > u_2 > 0.$$

The particle diffusion coefficient in the direction along the shock normal (x) is $\kappa = \kappa_{\parallel} \cos^2 \vartheta_{nB} + \kappa_{\perp} \sin^2 \vartheta_{nB}$, where κ_{\parallel} and κ_{\perp} are the components of the diffusion tensor along and across the field, respectively.

The general solution of this problem is well known and we will use it in the form of Blandford & Ostriker (1978):

$$f(x, p) = \begin{cases} f_{\infty}(p) + [F(p) - f_{\infty}] \exp \left[-u_1 \int_0^x \frac{dx'}{\kappa(x', p)} \right], & x \geq 0; \\ F(p), & x < 0. \end{cases} \quad (2)$$

Here $f_{\infty}(p)$ is the background CR distribution far upstream of the shock and $F(p)$ is that at its front and downstream. The upstream part of the solution grows sharply with momentum at sufficiently large x , owing to the growth of the diffusion coefficient κ with p . This behavior can produce the required bump if the prefactor $F - f_{\infty}$ properly depends on the momentum. The function f_{∞} is given by the background spectrum, while an equation for $F(p)$ may be straightforwardly obtained by integrating both parts of Eq. (1) across the flow discontinuity at $x = 0$:

$$p \frac{dF}{dp} + qF = qf_{\infty}, \quad (3)$$

where $q = 3r/(r - 1)$ with $r = u_1/u_2$ being the shock compression.

For the next step, it is convenient to write the solution as follows,

$$F = f_{\infty} - \int_0^p \left(\frac{p'}{p} \right)^q \frac{\partial f_{\infty}}{\partial p'} dp'. \quad (4)$$

We have merely assumed here that f_{∞} grows slower than p^{-q} as $p \rightarrow 0$, where the singularity at low energies is naturally removed by the diminishing flux of “aged” CRs due to the fast ionization losses (Strong & Moskalenko 1998).

Now we need to specify f_{∞} . If the solution in Eq. (2) correctly describes the observed CR spectrum, then at particle momenta below the first break, the exponential term is very small and we can derive f_{∞} from the observed spectrum in this energy range. Of course, we need to know it also at higher momenta where the spectrum is masked by the exponential term, presumably responsible for the spectral

¹ See, e.g., a bow shock around LL Ori in the Orion Nebula: <https://www.nasa.gov/multimedia/imagegallery/imagefeature1060.html>

feature. However, the spectrum below the first break is a simple power-law, $\propto p^{-\sigma}$, with the index measured to be close to $\sigma \approx 4.85$ (e.g., [Boschini et al. 2020b](#)). Assuming that it continues with the same slope $\sigma < q$, at least to the second break, we substitute this power-law into the solution for F in Eq. (4) to obtain the following relation,

$$\frac{F}{f_\infty} = 1 + \frac{\sigma}{q - \sigma}.$$

Now we can express the solution upstream through f_∞ :

$$f(x, p) = f_\infty \left\{ 1 + \frac{\sigma}{q - \sigma} \exp \left[-u_1 \int_0^x \frac{dx'}{\kappa(x', p)} \right] \right\}. \quad (5)$$

Note, that assuming the shock intrinsic index q being larger than that of the background CRs, $q > \sigma \approx 4.85$, implies a low-Mach shock. For that reason, we have not added the freshly injected CRs to the solution, but will discuss the implications of this omission in Sect. 5.1. In addition to being dominated by the background CRs at higher energies, as $q > \sigma$, they could not be injected efficiently in the first place (e.g., [Hanusch et al. 2019](#)), provided that the Alfvénic shock Mach number, $M_A \lesssim 2 - 3$. The second term in the solution in Eq. (5) represents the shocked background spectrum.

In most of the CR transport regimes the diffusion coefficient κ grows with momentum. Therefore, at some distance ahead of the shock only particles with higher momenta contribute to the second term in the above solution. It is this growth with momentum that produces the spectrum upturn at ~ 0.5 TeV. The growth, however, saturates at $p \rightarrow \infty$, and so the overall spectrum reestablishes its background profile, but at an enhanced level, $f \approx q(q - \sigma)^{-1} f_\infty$. This second transition is responsible for the spectrum softening at ~ 15 – 20 TV. The spectral shape thus has a required appearance of the observed CR bump and it very much depends on the following function of momentum, see Eq. (5),

$$\Phi(p) = u_1 \int_0^x \frac{dx'}{\kappa(x', p)}, \quad (6)$$

where the variable x is considered to be fixed, e.g., by the observer’s position.

Clearly, the presence of the two breaks in the spectrum requires the path integral Φ to vary between small and large values with momentum p (see Sect. 5.3 for details). This imposes a constraint on the distance $L \sim x / \cos \vartheta_{nB}$ from the shock to the observer. However, the integral along the particle propagation path runs through regions with different propagation regimes, between which κ varies by orders of magnitude. For sufficiently small particle momenta, $\Phi \sim 1$ is already in the shock precursor. If the CR intensity near the shock is sufficient to drive waves to the Bohm regime, $\delta B \sim B$, that is, $\kappa \sim cr_g$, which gives an estimate for the distance $L \sim r_g c / u_1$, where r_g is the proton gyroradius. For a TV rigidity of the spectral hardening (first break) and $u_1 \sim 10^{-3}c$, the estimate yields, as a lower bound, $L \sim 1$ pc. There are two questions about this estimate, though. First, if

the Bohm regime is realistic for the observed intensity of the CR excess. Second, if the $\kappa \propto p$ Bohm scaling fits its spectral shape. We address these questions in Sect. 5 and Appendix A, and the answer is negative for both questions. Therefore, we need to extend the integration in Eq. (6) beyond the shock precursor.

Far from the shock, we may try to substitute a popular ISM value for $\kappa_{\parallel} = 10^{28} (p/mc)^a$, with $a = 0.3 - 0.6$, neglecting the above contribution to the path integral from the shock precursor. We obtain the following upper bound on the distance to the observer:

$$L \sim 3 \cdot 10^2 \frac{\cos \vartheta_{nB}}{u_{100}} (p/mc)^a \text{ pc},$$

where u_{100} is the shock speed in units of 100 km s^{-1} , and p is the typical momentum of particles that form the bump. The caveat in this estimate is that the plane-shock solution becomes invalid upstream from the shock precursor. Even if we assume the most favorable Kolmogorov scaling with $a = 1/3$, the distance L for the TeV particles may reach a kpc scale. As we argue in Sect. 5.2, observing the sharp spectral breaks at such a long distance would be untenable because of the momentum diffusion. In addition, particles diffusing that far from the shock are unlikely to stay inside the flux tube and never return to the shock which is required for the solution in Eq. (5). We, therefore, conclude that neither lower nor upper bound on the distance is realistic.

A systematic approach to the path integral in Eq. (6) must thus include the effects of waves that are self-generated by the reaccelerated particles both near the shock and further along their path to the observer. We will address these processes in the next section. However, the rigidity dependence of the spectrum at the observation point can be obtained from Eq. (5) already at this point. As we will argue in the next section, one may approximate the path-integrated rigidity dependence of $\kappa(R)$ as $\kappa \propto R^a$, with a being the turbulence index less one. By also equating x to the observer’s location the rigidity profile of the solution in Eq. (5) can be represented as follows:

$$f(R) = f_\infty(R) \left[1 + K e^{-(R_0/R)^a} \right] \quad (7)$$

Here $K \equiv \sigma / (q - \sigma)$, while the parameters R_0 and a will be formalized in the next two sections before fitting the above equation to the data. We only note here that K is determined by the background CR index σ and the shock Mach number M , while R_0 depends on the distance to the observer, ζ_{obs} . Neither M nor ζ_{obs} are known, but we will constrain them using the fit, as the data set contains a sufficient amount of information for that. We emphasize that these are the only two parameters that are required by our model, while an ad hoc fitting of the bump spectrum requires six parameters: such as the two values of break rigidity, two widths of the breaks, and two changes of the spectral index at the breaks.

4. DISTANCE TO THE SHOCK, INTERVENING TURBULENCE, AND THE SPECTRUM

The goal of this section is to link the unknown shock distance, along with its other parameters, to the rigidity dependence of the path integral Φ in Eq. (10), which is observable. While the shock speed can be reasonably estimated, the dependence of Φ on the turbulence that scatters CRs is not known *a priori*. The level and the spectrum of this turbulence are the most important quantities that determine both the observed spectral anomaly and the distance to its source. The turbulence is generated by two different mechanisms, depending on how far from the shock the waves are excited. In the shock precursor, Alfvén waves are generated by the ordinary ion-cyclotron instability, usually employed in diffusive shock acceleration problems. Further out along the flux tube the turbulence is driven by the lateral pressure gradient of the shocked CRs.

Self-generated waves strongly suppress the particle diffusivity κ near the shock, but not necessarily down to the Bohm value, $\kappa_B = cr_g/3$, assumed in Sect. 3 for a crude estimate. The wave generation can be related to the pressure exerted by the shocked CRs along the tube through the work done on the waves, e.g., (Drury 1983):

$$(u + V_A) \frac{\partial E_w}{\partial \zeta} = V_A \frac{\partial P_{CR}}{\partial \zeta}, \quad (8)$$

where E_w and P_{CR} are the Alfvén wave energy density and the CR pressure, respectively, V_A is the Alfvén speed, $u = u_1 / \cos \Theta_{nB}$, and ζ is the coordinate running from the shock along the field line. It is related to the coordinate x used in Sect. 3 as $x = \zeta \cos \vartheta_{nB}$. Within the quasilinear approximation, the particle diffusion increases with ζ as $\kappa_{\parallel} \propto 1/E_w \propto 1/P_{CR}$, which we apply in the shock precursor. At larger ζ , where the cyclotron instability subsides, the quasilinear treatment has to be abandoned. Nevertheless, as long as the tube remains overpressured by the shocked CRs, κ_{\parallel} does not rise to the level of the background ISM, κ_{ISM} , in contrast to the quasilinear predictions. It remains at an intermediate level, κ_{int} , which is between the diffusivity near the shock and in the ISM, κ_{ISM} . Using Eqs. (1) and (8), in Appendix A we express the path integral in Eq. (6) through κ_{int} :

$$\begin{aligned} \Phi(p, \zeta) &= \ln \frac{P_{CR}(0)}{P_{CR}(\zeta)} \\ &\simeq \frac{u\zeta}{\kappa_{int}} + \ln \left[P_{CR}(0) \frac{\kappa_{int}}{\kappa_B} \left(1 + \frac{u}{V_A} \right)^{-1} \right]. \end{aligned} \quad (9)$$

Unlike in the shock precursor, where the excited Alfvén waves are rapidly swept up by the shock, the turbulence in the flux tube is long-lived and has enough time for transforming to different modes and cascading in the wave number. It supports the CR diffusivity at the level κ_{int} . Its contribution is roughly characterized by the first term on the r.h.s. in Eq. (9), but it requires a more accurate treatment. We show in Appendix B that the turbulence originates from an acoustic instability driven by the excessive CR pressure in the flux tube.

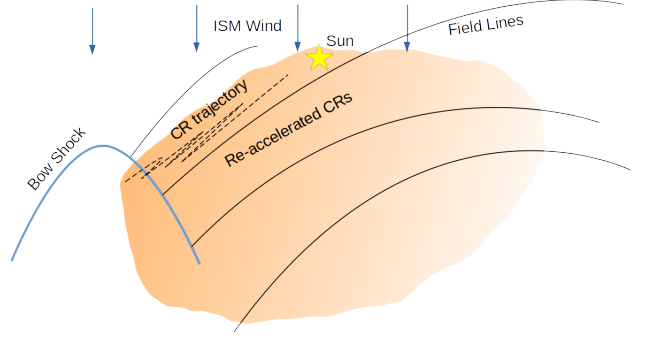


Figure 1. Schematics of a bow-shock ahead of a moving star and reaccelerated CRs, diffusing predominantly along the field lines.

Up to now, there was no need to specify the shock geometry, as we have used a one-dimensional model. To understand the excitation of the acoustic instability requires at least a two-dimensional approach. In Appendix B we consider a bow shock ahead of a moving star, Fig. 1, as a simple two-dimensional setup for the flux tube. The acoustic instability inverse-cascades to longer waves with a steep spectrum, $\propto k^{-3}$. It is, however, intercepted by a forward Alfvén cascade that results in the I-K turbulence, $k^{-3/2}$, thus yielding the $\kappa_{int} \propto \sqrt{p}$ -scaling with momentum. One can see then that at large ζ the first term on the r.h.s. of Eq. (9) varies in a much broader range than the second one, when the particle rigidity varies between the spectral breaks. Therefore, the main contribution to the path integral in Eq. (6) comes from the flux tube outside of the shock precursor, which is consistent with our preliminary estimates. Since $\kappa_{int}(\zeta, p)$ maintains the \sqrt{p} -scaling throughout this region we can write the value of Φ at the observation point $\zeta = \zeta_{obs}$, as a function of rigidity, R , as follows (cf. Eq. [7]):

$$\Phi(\zeta_{obs}, R) = \left(\frac{R_0}{R} \right)^{1/2}. \quad (10)$$

The quantity R_0 has a meaning of the bump rigidity, so that the spectral hardening occurs at $R \approx 0.1R_0$, while the softening – at $R \approx 4R_0$, Sect. 5.3. This quantity is calculated in Appendix C and is given (in units of GV) as:

$$R_0 = \left[3(\sigma - 3) \xi \frac{u}{c} \sqrt{2\eta\Gamma(2\sigma - 8)} \right]^{2/(\sigma - 3)} \text{ GV}. \quad (11)$$

Together with the shock index, q , in Eq. (5), R_0 fully determines the shape of the spectrum. Apart from the measured CR background index $\sigma \approx 4.85$, and the shock velocity u , it depends on the following two dimensionless parameters:

$$\xi \equiv \frac{\zeta_{obs}}{\sqrt{r_{GV} l_{\perp}}} \quad \text{and} \quad \eta = \frac{KP_{\infty}}{\rho C_s V_A} \frac{\sigma - 4}{R_*^{4-\sigma}}, \quad (12)$$

which are the normalized distance to the shock, and the pressure of accelerated CRs η , normalized to the geometric mean of thermal and magnetic pressure in the ISM (see Eq. [C18]). Here l_{\perp} is the characteristic transverse scale of the flux tube and r_{GV} is the gyroradius of a GV proton.

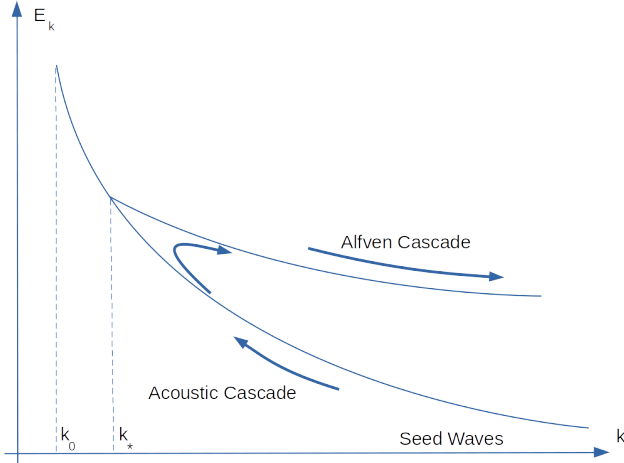


Figure 2. Acoustic wave energy cascading to longer scales until they are intercepted by the Alfvénic forward cascade.

This concludes our theoretical consideration of reacceleration and propagation of CRs to the observer. Our predictions thus depend on several unknown parameters: the distance and the size of the shock (roughly equivalent to l_\perp), the shock Mach number, M , and the shock speed, u . The latter two can be related if the temperature of the ISM near the shock is known. In fact, however, to make a precise comparison of our model predictions with the observed spectrum, the following two parameters suffice, the shock Mach number (to determine its index q) and R_0 . Courtesy of the I-K turbulence spectrum, derived on theoretical grounds, our model thus contains no free parameters. Therefore, even though the physical parameters of the shock and its geometry are not known, we can determine M and constrain other physical parameters by obtaining R_0 from the best fit to the data.

5. FITTING THE DATA

Unlike the common practice to compare theoretical predictions with discrete sets of data, we compare our prediction with a continuous version of the observed proton spectrum. The latter has been provided by [Boschini et al. \(2020b\)](#), in a convenient form of analytic fit to the actual multi-instrument data set. We will ignore individual instrumental errors, as the cumulative data-set significantly diminishes them. The analytic expression is rather cumbersome and contains ten fitting parameters to accurately represent the local ISM CR spectrum; we show it plotted in Fig. 3. We denote this spectrum by $f_d(R)$ and compare with our two-parameter (M and R_0) prediction in Eq. (13). To this end, we rewrite Eq. (7) in the following form:

$$f(R) = 2.3 \times 10^4 R^{-0.15} \left[1 + K e^{-(R_0/R)^a} \right], \quad (13)$$

where $K(M) \equiv \sigma/(q - \sigma)$ (see below) and R_0 is defined in Eq. (11). Here the CR density $f(R)$ is normalized to $f dR$, as opposed to $f p^2 dp$ in Eq. (5). Also, following a common

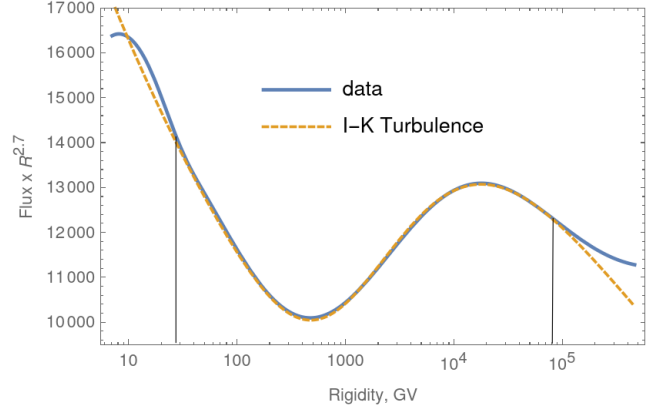


Figure 3. Fit of the diffusive shock acceleration result in Eq. (13) (dashed line) to the CR proton data compilation by [Boschini et al. \(2020b\)](#) (solid line). The region between the vertical lines is physically related to the shock acceleration in the Local Bubble and is used to calculate the relative deviation between the two curves presented in Eq. (14). Here we used $a = 0.515$, $K = 2.39$, $R_0 = 4434$ GV.

practice, we have multiplied f by an additional factor $R^{2.7}$ to make the spectral structure visible. The normalization factor and the power-law index (0.15, stemming from the CR background index $\sigma = 4.85$, introduced in the previous section) are fixed by comparing the background CR spectrum f_∞ in Eq. (5) with the synthetic data, $f_d(R)$, from [Boschini et al. \(2020b\)](#). We match the two at lower rigidities, $R \ll R_0$, where the shock does not perturb the spectrum near the heliosphere.

Although we have calculated the CR diffusion coefficient, $\kappa(R) \propto R^{1/2}$ in Appendix C, we introduced an additional parameter a in Eq. (13) to investigate if other turbulence models may also apply. The nominal value is thus $a = 1/2$, but we will explore the Kolmogorov ($a = 1/3$) and the Bohm ($a = 1$) models as well. The former is believed to be suitable for the CR transport in the Galaxy, while the latter is expected to dominate near the shock front ([Bell 1978](#)) and it also occurs in the solar wind turbulence ([de Wit et al. 2020](#)). We will scan the parameter space by changing a in the range $a = 0.2 - 1.0$ and also determine $K \equiv \sigma/(q - \sigma)$ and R_0 by minimizing the deviation of the model prediction from the data. However, first we find the absolute minimum of this deviation which happens to correspond to $a = 0.515$ that is slightly larger than the nominal I-K value.

Shown in Fig. 3 is a nearly perfect match between the data and our model, found for $K = 2.39$ and $R_0 = 4434$. By defining the relative deviation between the two curves as

$$\Delta = \int_{R_1}^{R_2} |f - f_d| dR \bigg/ \int_{R_1}^{R_2} f_d dR, \quad (14)$$

where f_d is the “data,” and $R_1 = 28$ GV and $R_2 = 8 \times 10^4$ GV are chosen to contain the shock-related perturbation of the spectrum. The bump rigidity R_0 satisfies the relation $R_1 \ll R_0 \ll R_2$. Using the above formula, we have com-

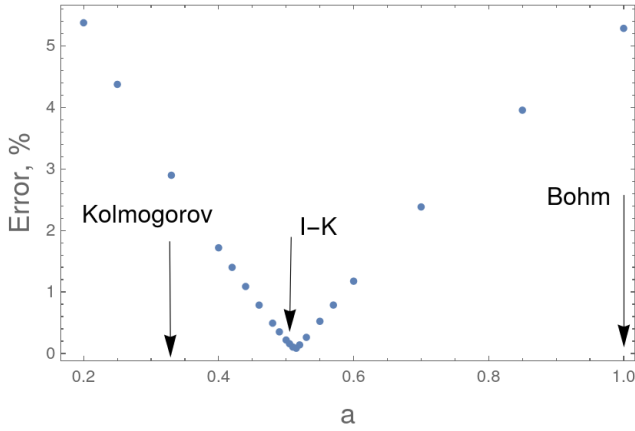


Figure 4. The calculated deviation of the predicted spectrum from the synthetic data vs. the index of the diffusion coefficient, Eq. (14). The indices corresponding to the Kolmogorov, I-K, and Bohm diffusion are shown by arrows.

puted that $\Delta \approx 8.5 \times 10^{-4}$. We discuss the incipient discrepancies between the two spectra outside of this range in Sect. 5.1. An insignificant shift in a from $1/2$ might be produced by a minor contribution of the Bohm scaling, $\propto p$, near the shock, not included into the path integral. It can equally well be attributed to the observation errors, and should generally be ignored in any realistic choice of the underlying turbulence model.

The sensitivity of our model predictions to the turbulence regime is demonstrated in Fig. 4 that shows a scan of the function Δ in the turbulence parameter a . Clearly, the I-K model stands out reaching a sharp minimum of the error Δ very close to $a = 1/2$. In fact, even at the exact I-K value $a = 1/2$, the error is about 0.2% , and, as we mentioned, even that minuscule deviation from the nominal I-K index can still be consistent with the model. To demonstrate that the I-K is by far the most likely turbulent regime in the flux tube we plot in Fig. 5 the model prediction for the Kolmogorov turbulence with $a = 1/3$. This is the nearest to the I-K spectral index (from the two shown in Fig. 4), but the disagreement with the data is significant. In particular, it over-predicts the bump position by a factor 2-3 and is inconsistent with the newest data even if the error bars are included.

The CR bump amplitude $K \approx 2.39$ implies the shock power-law index $q \approx 6.88$, which translates into the shock compression $r \approx 1.77$, and then into the Mach number $M \approx 1.55$. Note that these parameters formally relate to the scattering centers in the shock precursor, which may move with the Alfvén speed V_A backward with respect to the inflowing plasma. However, this is quite uncertain as we do not know the shock angle, the turbulence level and the plasma β . These factors can change the wave dispersive properties. For example, if the turbulence level is sufficiently high, the induced scattering of waves on thermal ions or other nonlinear processes, such as interaction with magneto-acoustic waves, may symmetrize the Alfvén waves in terms of the propagation direction, thus making them effectively frozen into the

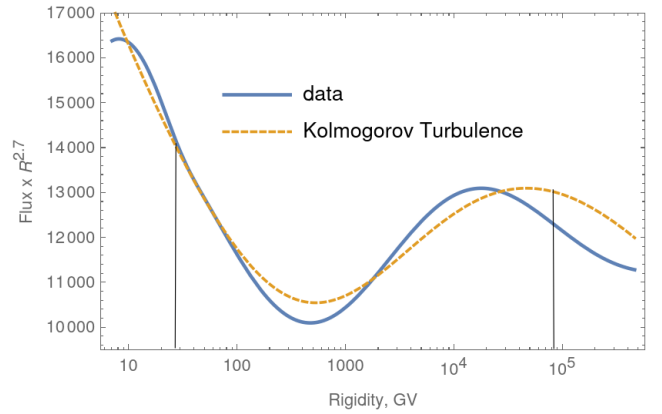


Figure 5. Same as in Fig. 3, but for Kolmogorov turbulence with $a = 1/3$. The best agreement is at $K = 3.73$, $R_0 = 15665$ GV.

flow. The latter was assumed in the above calculations for simplicity.

Unlike K , which is fully determined by the shock compression, the second model parameter, R_0 , depends on the unknown distance to the shock, its size, and speed. In order to constrain these quantities, we first calculate the shock speed u from the shock Mach number, $M \approx 1.55$, obtained from the best fit value of $K \approx 2.4$. Its upper bound may be placed by taking the temperature in the Local Bubble $T \simeq 10^6$ K (e.g., Snowden et al. 2014), which gives $u_1 \simeq 150$ km s $^{-1}$. In denser and cooler regions the speed is several times lower. Also, small density clumps in the ISM effectively reduce the shock speed.

We can now substitute the parameters K and R_0 , inferred from the data, in the expression in Eq. (C19) for the normalized distance ξ , while setting $R_* \approx 1$:

$$\frac{\zeta_{\text{obs}}}{\sqrt{r_{\text{GV}} l_{\perp}}} \approx 2 \times 10^2 \frac{c}{u} \sqrt{\frac{\rho C_s V_A}{P_{\infty}}}. \quad (15)$$

To get a crude estimate, we can substitute $r_{\text{GV}} = 10^{12}$ cm, $c/u \sim 3 \times 10^3$, and the normalized CR pressure $P_{\infty}/\rho C_s V_A \approx 1$ into Eq. (15). Then, we obtain $\zeta_{\text{obs}} \sim 10^2 \sqrt{l_{\perp}}$, where the both lengths, ζ_{obs} and l_{\perp} , are given in pc.

The value of l_{\perp} is still uncertain. In contrast to ζ_{obs} , however, we can constrain it by assuming that the shock is a bow shock of a moving star, and its size is not much larger than our own heliosphere, even if we leave a room for the reaccelerated CR to form a wake. Inserting then $l_{\perp} \sim 10^{-2}$ pc into the last estimate, we obtain an upper bound on $\zeta_{\text{obs}} \sim 10$ pc. A lower bound on l_{\perp} can be obtained if the Sun is just entering the flux tube, as shown in Fig. 1. In this case, l_{\perp} is the scale of the edge of the flux tube rather than its full radius. We will discuss the implications of this scenario for the time-dependent CR spectrum, observed locally. In any event, l_{\perp} cannot be smaller than the gyroradius of those reaccelerated CRs that make the main contribution to their pressure. Formally this quantity is as small as r_{GV} , but particles with such small gyroradii do not diffuse far from the shock and a

more plausible estimate is the gyroradius of particles with the rigidity corresponding to the spectral upturn, that is ~ 1 TV. This estimate yields $l_{\perp} \sim 10^{15}$ cm and, therefore, a few pc for ζ_{obs} . Based on our estimates of l_{\perp} in Eq. (B12), a moderate inverse cascade of Alfvén waves might be required to allow for such a short l_{\perp} . We thus conclude that the distance to the reaccelerating bow shock is likely in the range 3–10 pc.

5.1. Spectrum Beyond the Excess Region

Our model spans the rigidity range $30 < R < 10^5$ GV, Fig. 3. Beyond each end of this interval, the model under-predicts the data. Both below $R = 30$ GV and above $R = 10^5$ GV the spectrum is likely to be unrelated to the shock in question. Nonetheless, we briefly discuss how our model can be extended to these intervals.

A moderate enhancement of the data above the model prediction at the lower rigidities can be due to freshly injected primaries. We have neglected their contribution to a broad bump in the spectrum in the 10 TV range, because the shock is weak, thus producing much steeper spectrum (index $q \approx 6.9$) than the background spectrum (index ≈ 4.9). For precisely that reason, however, the contribution of these particles at lower energies can be increasingly visible. They must have much higher density near the shock than the reaccelerated particles. Therefore, by penetrating the magnetic flux tube, even in a small number, these particles may partially survive the upstream screening effect in Eq. (2) and reach the Sun. Apart from the injection, ionization energy losses may also distort the spectrum of aged CRs at lower rigidities.

The deviation of the fit from the data at $R > 10^5$ GV can be explained by a possible slight concavity of the CR background spectrum f_{∞} that we have substituted in the shock solution as a straight power law. In reality, however, while the spectrum between $30 < R < 10^5$ GV is dominated by the reacceleration at the bow shock, the underlying background spectrum may flatten between these limits. At higher rigidities the shock reacceleration stops working, because the acceleration time, κ/u^2 , approaches the shock convection time, l_{\perp}/u , available for the reacceleration. At higher rigidities the background spectrum reemerges with a flatter slope than it has below the first break. The flattening is consistent with the CR spectrum behavior at sub-knee rigidities.

5.2. Momentum Diffusion

Propagation of reaccelerated CRs to the Sun through an enhanced turbulence comes with their enhanced diffusion in momentum. The required bi-directional Alfvén wave spectrum is justified by the genesis of these waves in the acoustic instability discussed in Appendix B. Hence, relatively sharp kinks in the observed spectrum may constrain the distance to their source, in addition to the estimate in Eq. (15). It is convenient to employ the following inverse relation between the particle diffusivity in momentum, D_{pp} , and that along the field, κ_{\parallel} , with a numerical factor justified by Drury & Strong

(2017):

$$D_{pp} \simeq 0.1 \frac{V_A^2 p^2}{\kappa_{\parallel}}.$$

By noting that the spreading in momentum for the particles traversing the distance ζ_{obs} from the source is $\Delta p^2 \sim D_{pp} \zeta_{\text{obs}}^2 / \kappa_{\parallel}$ and combining the above relation with Eq. (15) and (C14) with $P_{\text{CR}}/P_{\infty} \sim 1$ at large distances from the shock, we find the relative rigidity spreading:

$$\frac{\Delta R}{R} \sim 10^2 \frac{V_A}{u} \sqrt{\frac{1 \text{ GV}}{R}}.$$

This broadening of the peak at $R \sim 10^4$ GV in Fig. 3 is not large, especially if the plasma β is high, so $V_A \ll u$. It may become closer to unity at the spectral minimum around $R \lesssim 10^3$ GV. Nevertheless, the minimum breadth is not in tension with the $\Delta R \sim R$ result. In addition, the above estimate gives an upper bound on the momentum diffusion as it does not include the convective screening of low-energy particles and a possibly asymmetric wave propagation.

The above estimate of ΔR merely assumes that particles reaccelerated at the shock diffuse in ζ -direction, while also diffusing in momentum. To account for the momentum diffusion more accurately, it should be included in the particle transport in Eq. (1). If a sharper first break reported by CALET prevails over other instruments, this modification of the model may become desirable. Note, however, that other instruments, particularly DAMPE that also claims high precision at the first break rigidity, currently indicate a smoother than CALET transition (see, e.g., Lipari & Vernetto 2020 for the recent multi-instrument data compilation).

5.3. Possible Time Dependence Due to the Spatial Gradient

For our estimate of the distance to the bow shock in Eq. (15) to be plausible the CR pressure profile must be sufficiently steep in the cross-field direction. Our analysis in Appendix C suggested that the lateral gradient scale l_{\perp} must be in the range $10^{15} - 10^{16}$ cm. When the Sun crosses the flux tube of that scale then the CR variation can be detectable. If the relative velocity between the bow shock and the Sun is $\sim 100 \text{ km s}^{-1}$, as the fit suggests, then the relevant crossing time is $\tau \sim 3 - 30$ yr, which merits a closer look at the historical data.

Early reports on the spectral hardening date back to the ATIC-2 paper (data taken in 2002–2003, Ahn et al. 2006), first two flights by CREAM (data taken in 2004–2005, Ahn et al. 2010), and first two years of PAMELA data (data taken in 2006–2008, Adriani et al. 2011). The position of the first break (hardening) was significantly lower, $\sim 200 - 240$ GV vs. its current value of 450 GV from AMS-02 proton data (Aguilar et al. 2015a), although the uncertainties are large. The situation with the second break (softening) is much less clear. According to the current fit, it is at 17 TV, which is, however, based on a multi-instrument compilation with even larger uncertainties. There is no PAMELA data in this range, while the ATIC-2 data (2002–2003) are more consistent with a ~ 10 TV break, but the statistical errors are quite large.

Table 1. The model and problem parameters

Notation	Description	Theoretical prediction	Best fit value	Measured value
s	k^{-s} turbulence index	3/2	1.49	...
ζ_{obs}	Distance to the bow shock	3–10 pc
$\xi \equiv \frac{\zeta_{\text{obs}}}{\sqrt{r_{\text{GV}} l_{\perp}}}$	Normalized distance	Eq. (15)
$\eta = \frac{K P_{\infty}}{\rho C_s V_A} \frac{\sigma - 4}{R_*^{4-\sigma}}$	Normalized background CR pressure
$R_0/1 \text{ GV} = \left[3(\sigma - 3) \xi \frac{u}{c} \sqrt{2\eta \Gamma(2\sigma - 8)} \right]^{2/(\sigma - 3)}$	CR Bump rigidity, GV	...	4434	...
σ	Index of background CR spectrum	4.3–4.6 ^a	...	4.85 ^b
$K \equiv \sigma / (q - \sigma)$	CR Bump magnitude	...	2.4	...

^aIndex, generally expected for CRs accelerated in SNRs and propagated in Kolmogorov turbulence with $a \approx 0.3$ (see text).

^bIndex, extracted from multi-instrument data around ~ 100 GV, presumably propagated through the flux tube in I-K turbulence.

Let us now turn to the solution parameters K and R_0 in Eq. (13) (with $a = 1/2$) that determine the two breaks whose rigidities we denote by R_h and R_s , where ‘h’ and ‘s’ stand for hardening and softening, respectively. The K -value must change with time, as it is proportional to the CR excess. Note that the one-dimensional solution in Eq. (13) does not include the cross-field variation of the CR flux, so K formally depends only on the shock index q and the background CR index σ that are constant. The one-dimensional approximation applies only well inside the flux tube, where the CR flux reaches its maximum. The second parameter, R_0 , clearly changes across the flux tube as it directly relates to the turbulence enhancement. By looking for the extrema in Eq. (13) we can derive the following simple equation for R_h and R_s :

$$\frac{\sqrt{R_0/R}}{0.3} = 1 + e^{\sqrt{R_0/R} - \ln K}.$$

We see that the both roots of this equation scale linearly with R_0 , but only logarithmically depend on K . The current value of $K = 2.4$ is not big enough to neglect the variations in $\ln K$ completely. Nevertheless, we justify this step by noting that had K changed strongly over the time, its value would be too close to the background CR intensity back in 2002–2008 and the excess would have not been detected.

The parameter R_0 varies across the tube with the turbulence level, Eq. (C15), which we expressed through the CR pressure, P_{CR} . After fixing $K = 2.4$, from the equation above we find:

$$R_h \approx 0.1 R_0 \propto P_{\text{CR}},$$

while $R_s \approx 4 R_0$. From here we conclude that, indeed, R_h may have increased by a factor of two (from ~ 230 GV measured by ATIC and PAMELA) to the current value of 455 GV over 10–15 yrs, provided that the Sun penetrated deeper into the flux tube and the turbulence level increased by the

same factor. The second break at $R = R_s$ must have increased proportionally to R_h , unless the turbulence index a also changed over the time. This change cannot be ruled out, since well outside of the tube a more likely value, based on the B/C ratio, derives from the Kolmogorov turbulence with $a \approx 1/3$, rather than the I-K index that we have arrived at. On the other hand, the argument about the detectability applied to the parameter K seems to be applicable to a as well.

We note that the drift in the opposite direction, i.e. the decrease of the break rigidity with time is also possible, and depends on the configuration of the magnetic tube and orientation of the shock relative to the Sun. We shall return to the possible variability of the CR bump in Sect. 8.

6. PASSING STARS

However accurate the spectral fit may be, our model’s success depends on identifying the object most likely responsible for the spectral bump. It did not take long to find two passing stars, which perfectly match the derived range of distances and velocities: the binary Scholz’s Star at 6.8 pc distance with the radial velocity 82.4 km s^{-1} , and a triple system Epsilon Indi at 3.6 pc that has the radial velocity -40.4 km s^{-1} and a considerable proper motion. These are just two examples indicating that such passings within a few pc distance are not unusual. We start with a brief discussion of their physical properties and turn to the critical question of their magnetic connectivity with the heliosphere afterward.

The recently discovered Scholz’s Star (Scholz 2014) is a system of red M9.5 and brown T5.5 dwarfs (Mamajek et al. 2015) with masses of $0.095 M_{\odot}$ and $0.063 M_{\odot}$, correspondingly. The system has a moderately eccentric orbit $e = 0.240$ with a semi-major axis of ~ 2 au, and a period of 8 yr (Dupuy et al. 2019) that amended the previous estimate of Burgasser et al. (2015). The Scholz’s Star has passed within the close proximity of the Sun, 0.25 pc, about 70–80 kyr ago, and is

moving away from us. Therefore, the Sun is located downstream in its system.

The peculiar proper motion of the Epsilon Indi system was noticed already about two centuries ago (D’Arrest 1847). The main star A in the Epsilon Indi system is a K4.5V star² with mass $\sim 0.77 M_{\odot}$. The recently discovered two smaller stars B and C belong to the brown dwarf family with classes T1.5 and T6 and masses of $0.072 M_{\odot}$ and $0.067 M_{\odot}$, correspondingly (Dieterich et al. 2018). The main star and the binary brown dwarf system are separated by ~ 1500 au. The Epsilon Indi star is moving toward us with the Sun located upstream.

Both star systems can generate multiple colliding bow shocks with rich opportunities for particle acceleration (e.g., Bykov et al. 2019): (i) Each companion star produces its individual bow shock, (ii) The shock velocities are modulated with the orbital motion, and (iii) the tight separation in each system ensures that the shocks are colliding and amplifying each other. In the case of the Scholtz’s star, a combination of the directed and orbital motion (with period τ) produces downstream magnetic and kinetic perturbations with the wavelengths $\lambda_B \sim V_A \tau \sim 10^{14} - 10^{15}$ cm and ~ 2 au $\approx 3 \times 10^{13}$ cm, respectively. They are relevant for the scattering and confinement of CRs with up to TV rigidity. Moreover, the orbital motion injects magnetic and kinetic helicity into the turbulence past the star systems, which is necessary for an inverse MHD cascade (Pouquet et al. 1976; Pouquet et al. 2018). Even though we have considered the propagation of reaccelerated CRs upstream of a shock, the turbulence left behind by the Scholtz’s star may have important implications for our model. It can provide an enhanced scattering and confinement of particles at the rigidities beyond the TV range.

The model we discussed in the paper can be applicable to the Epsilon Indi system. Epsilon Indi must have a bow shock that is very much different from the ordinary one formed by a single star. A 1500 AU separation, 11-yr orbital period, and colliding stellar winds inject much more turbulent power than the Scholtz’s star does. All this happens downstream of the bow shock and has no direct impact on the reaccelerated CRs upstream. However, the reacceleration process may be enhanced, and the bow shock is likely to be rippled due to the stellar dynamics behind it. An exciting, but speculative, aspect of this dynamics is a possible 11-yr variations in the CR bump parameters. Here the coincidence with the solar cycle period is accidental, as our Sun maintains this period for hundreds of millions of years (Luthardt & Roessler 2017).

Meanwhile, even slower moving stars, such as the Epsilon Eridani² (~ 20 km s⁻¹), may be viable candidates. Epsilon Eridani star at a distance of 3.2 pc is the closest of the three and fits well within the derived range of distances. It is a K2 dwarf with a mass of $0.82 M_{\odot}$, a radius of $0.74 R_{\odot}$, and an effective temperature of ≈ 5000 K (Baines & Armstrong 2012). Nevertheless, it has a high mass loss rate of $30 \dot{M}_{\odot}$

and a full width of its astrosphere reaches about 8000 au with the corresponding angular size $\sim 42'$ (larger than the Moon!) as viewed from the Earth (Wood et al. 2002).

Higher speed through the ISM implies faster particle acceleration and a longer flux tube with reaccelerated CRs. These CRs may then reach the Sun before they dissolve in the ISM. Alternatively, a slower shock in a cooler phase of the ISM (e.g., warm ionized medium, or WIM with $T \sim 10^4$ K) may produce a similar spectrum, albeit at a slower pace and suppressed CR self-confinement due to ion-neutral collisions. A large shock, similar to that of the Epsilon Eridani star, may compensate for these drawbacks. These considerations widen the choice of suitable objects in the solar vicinity.

7. ANISOTROPY FROM MAGNETICALLY CONNECTED CR SOURCE

Perhaps the most compelling evidence for the CR bump association with a nearby star might come from the star fortuitously found in the same flux tube with the heliosphere. There are only a handful of stars with suitable characteristics within 10 pc around the Sun. Therefore, the chances are very much against its existence. Nevertheless, Epsilon Eridani appears to be the *one*. It is only a small turn of $\approx 6.7^\circ$ away from the local magnetic field direction, and as already mentioned, it is located at 3.2 pc away from the Sun and possesses a huge astrosphere.

In Sect. 8, we discuss the topology of the local magnetic field and its perturbation mechanisms, whereby may increase the probability for other stars to be connected to the Sun. However, the Epsilon Eridani stands out in that all it takes for it to be magnetically connected to the Sun is just a straight field line. If we assume this simple field configuration, two implications follow: the obvious one is that the star is indeed exceptional. The chance to find a suitable candidate star no further than 6.7° off of the local field direction is only $\approx 0.3\%$, assuming that its position on the sky is random. To evaluate the total probability of this fortunate outcome, we sample 3-4 stars that have detectable astrospheres (bow shocks) of a size > 1000 au (to exceed a 10-TeV CR Larmor radius) within 5 pc of the Sun listed by Wood et al. (2002). The probability of at least one of them to be found in such a narrow solid angle is not larger than one percent. This observation makes the bump no longer surprising. Indeed, the “standard” CR acceleration and propagation models that predict featureless spectra do not typically include such sources.

The second implication is that the source proximity is likely to produce imprints in the CR arrival directions other than a generally expected large-scale anisotropy. The latter can result from uneven distribution of sources in the Galaxy, for example, unrelated to the rigidity bump phenomenon studied in this paper. Historically, the discovery of a small-scale CR anisotropy in 1-10 TeV range, or “hot spots,” predated the rigidity bump discovery. The Milagro observatory (Abdo et al. 2008) reported a surprisingly sharp, $\sim 10^\circ$ anisotropy at a 10^{-4} level of the dominant isotropic CR component, atop the large-scale anisotropy at the 10^{-3} level. The observatory was decommissioned in 2008. Among its re-

² <http://www.astro.gsu.edu/RECONS/TOP100.posted.htm>

sults, was also a hardening of the CR proton spectrum associated with the sharp anisotropy spots. We retrospectively link these data with other early indications of the 10-TeV rigidity bump, discussed in Sect. 5.3.

The anisotropy spots have been observed later by several other instruments. An update of post-Milagro results can be found, e.g., in Ahlers & Mertsch (2017). They are in reasonable agreement with the original Milagro findings. However, the difference in the width of the small-scale structures and their relative position on the large-scale angular profile are noticeable. A number of factors may have caused the difference, such as different types of instruments, data processing, or even a putative time dependence of the CR spectrum in the TeV range, discussed in Sect. 5.3.

Unlike in our study of CR reacceleration in Sect. 3, we need to include the pitch-angle dependence of reaccelerated CRs, which makes the problem more difficult. Therefore, we split it in two parts: we consider the acceleration part of the problem as solved, and study the CR propagation along the source's flux tube. We take a step back from the rigidity spectrum obtained in Sect. 3 and assume a generic source with given momentum and pitch-angle distribution. For a high mass-loss but slowly moving star, its wind termination shock might reaccelerate CRs more efficiently than its bow shock. Having the Epsilon Eridani in mind, we further simplify the problem using its relative motion to the local gas at 76° to the line of sight (Wood et al. 2002). Since the latter is close to the local field direction, we may neglect the source motion along the field. With this additional symmetry, the following Fokker-Planck equation is suitable for the CR propagation along the field:

$$\frac{\partial f}{\partial t} + c\mu \frac{\partial f}{\partial \zeta} + \nu'_\perp f = \frac{\partial}{\partial \mu} (1 - \mu^2) D(p, \mu) \frac{\partial f}{\partial \mu} + Q(p, \mu) \delta(\zeta). \quad (16)$$

Here μ is the pitch angle cosine of a particle with momentum p . The spatial coordinate ζ is directed along the field, and the source is at the origin. The other two coordinates are removed by averaging the distribution function across the flux tube. The particle flux through its boundary (arising from an integral endpoint in averaging) is simplified to the form of $\nu'_\perp f$ on the l.h.s. (e.g., Malkov & Aharonian 2019). The CR scattering frequency D can be related to the Alfvén fluctuation energy density E_k^A , determined in Eq. (B11), using the standard quasi-linear formula (Kulsrud & Pearce 1969):

$$D = \frac{\pi^2 c}{|\mu| r_g^2 B_0^2} \rho_0 E_k^A \Big|_{k=1/r_g|\mu|} \equiv 4\nu_{\text{IK}}(p) |\mu|^{1/2}, \quad (17)$$

where we have specified the scattering frequency using the I-K spectrum obtained in Appendix B, Eq. (B11):

$$\nu_{\text{IK}} = \frac{\pi}{16} \sqrt{\frac{\gamma_D}{V_A r_g}}.$$

We represent the source term in Eq. (16) as follows: $Q = \nu_{\text{IK}} Q_0(p) Q_1(\mu)$, where $Q_1(\mu) = Q_1(-\mu) \approx \text{const}$, using

the problem reflection symmetry, $\zeta \rightarrow -\zeta$. Most of the above restrictions can be relaxed at the expense of more algebra in treating the transport problem below, but largely without new insight. We, therefore, continue to transform Eq. (16) by introducing dimensionless time and coordinate, and absorbing the source momentum dependence $Q_0(p)$ into f as follows:

$$\nu_{\text{IK}} t \rightarrow t, \quad \frac{\nu_{\text{IK}}}{c} \zeta \equiv \frac{\zeta}{\lambda_{\text{CR}}} \rightarrow \zeta, \quad \frac{f}{Q_0} \rightarrow f. \quad (18)$$

Next, we remove the $|\mu|^{1/2}$ -singularity from D by changing the variables:

$$\chi = |\mu|^{1/2} \text{sgn}(\mu).$$

However, we will demonstrate that the $|\mu|^{1/2}$ -suppression of particle scattering at the 90° pitch angle has a profound observable effect on the solution of Eq. (16). Assuming a steady state we transform Eq. (16) to the following equation:

$$\frac{\partial}{\partial \chi} (1 - \chi^4) \frac{\partial f}{\partial \chi} - \chi^3 \frac{\partial f}{\partial \zeta} - \nu_\perp f = Q_1(\chi) \delta(\zeta) \quad (19)$$

where $\nu_\perp \equiv |\chi| \nu'_\perp / \nu_{\text{IK}}$. It is also reasonable to assume that the lateral particle escape from the tube is symmetric, $\nu_\perp(-\chi) = \nu_\perp(\chi)$. The solution of the last equation has then the following cross-symmetry, $f(-\zeta, \chi) = f(\zeta, -\chi)$. By making use of it, the solution can be written in the following compact form for $\zeta \neq 0$:

$$f(\zeta, \chi) = \sum_{n=0}^{\infty} C_n f_n[\chi \cdot \text{sgn}(\zeta)] e^{-\lambda_n |\zeta|}. \quad (20)$$

Further details of this solution can be found in Appendix D. Below, we summarize the salient features of it.

The lowest eigenvalue $\lambda_0 \rightarrow 0$, for $\nu_\perp \rightarrow 0$, thus yielding a fully isotropic solution at $|\zeta| = \infty$. Furthermore, for any $\nu_\perp > 0$, $f \rightarrow 0$ for $|\zeta| \rightarrow \infty$. The eigenvalues λ_n with $n \geq 1$ are almost independent of $\nu_\perp \ll 1$. We assume this inequality to be strong. Were it not so, CRs from the star would not reach the Sun because of a strong lateral escape from the flux tube. While $\lambda_0 \ll 1$ (for vanishingly small ν_\perp), the next eigenvalues $\lambda_1 \simeq 45$, $\lambda_2 \simeq 130, \dots$ continue to grow rapidly with n . The solution of Eq. (19) is thus determined by the first n terms of the series in Eq. (20), where $\lambda_n \sim 1/|\zeta|$.

According to Sturm's oscillation theorem, the last condition limits the CR anisotropy scale from below, since the number of zeros of f_n is n . It is also worth noting that the zeros are on the positive side of χ -axis for positive eigenvalues λ_n for $n \geq 1$ and on its negative side for negative eigenvalues, $-\lambda_n$. Because of this difference, the full solution in Eq. (20) possesses the following observable property. It develops the small-scale anisotropy only for the particles moving away from the source. The returning particles exhibit only a large scale anisotropy. If they are a few mean free paths away from the source, then they have already scattered by a large angle, so their angular distribution is smooth. An exception to this rule are particles moving close to the

90° pitch angle, which merits a separate discussion later in this section and in Appendix D.

We show the first three eigenfunctions in Eq. (20) with $n = 0, 1, 2$ in Fig. 6. The “ground-state” f_0 carries the dominant isotropic part of the solution in the series in Eq. (20) and the bulk of its large scale anisotropy. It can be decomposed approximately as follows $f_0(\chi) \approx A + A'\chi = A + A'|\mu|^{1/2} \text{sgn}(\mu)$. The constants A and A' may be related using Frobenius expansions at the endpoints $\chi = \pm 1$. Neglecting small terms $\sim \nu_\perp \ll 1$, to the first order in $\lambda_0 < 1$, the expansions yield $A'/A \approx \lambda_0/4$ at the both endpoints. To this order, the constant A comes from the normalization condition, $\|f_n\|^2 \equiv (f_n, f_n) = 1$, that results in $A \approx \sqrt{5/\lambda_0}$ and then $f_0 \approx \sqrt{5/\lambda_0} + \sqrt{5\lambda_0}\chi/4$. (See Appendix D, as needed, for notation.)

From these considerations, we see that the anisotropy at some distance from the source, where $\lambda_1|\zeta| \gtrsim 3$, approaches $\approx \lambda_0/4$, regardless of its origin: be it the source, the CR losses from the flux tube, or both. The linear (in χ) anisotropy component should be detectable in the flux tube as long as $\lambda_0|\zeta| \lesssim 2 - 3$, depending on the strength of the source. More elaborate algebra with the Frobenius series at the endpoints and matching them inside of the interval $\chi \in (-1, 1)$ leads to the following dependence of $\lambda_0(\nu_\perp)$:

$$\lambda_0 \approx 2\sqrt{5\nu_\perp}. \quad (21)$$

It is formally valid for $\nu_\perp \ll 1$, but remains accurate even when λ_0 exceeds unity, which we illustrate in Fig. 7. This simple relation establishes the range of source visibility and anisotropy with no need to solve the full propagation problem.

The small-scale anisotropy ($f_{n \geq 1}$) can be observed at the dimensionless distance to the source $\lambda_1|\zeta| \lesssim 1$. To illustrate the variation of small- and large-scale anisotropy with the distance to the source, we show in Fig. 8 the angular distributions of CRs at three different $|\zeta|$. For ζ varying by only a factor of three, the CRs change their smooth dipolar anisotropy at longer distances to a sharper anisotropy when they are closer to the source. An observer approaching the source would also see progressively field-aligned CRs.

A more robust feature of the solution can be seen by using the conventional angular variable μ instead of χ . This feature becomes visible at distances $|\zeta| > \lambda_1^{-1} \approx 0.05$, where the sharp anisotropy near the field direction decays. Note, that λ_1 is practically independent of the lateral losses ν_\perp . The solution is dominated by f_0 (smooth at $\chi = 0$), but changes at $\mu = 0$ very sharply. This is a direct consequence of the I-K turbulence, already confirmed by the fit of the rigidity spectrum, independent of the anisotropy. The effect would be absent in the Bohm diffusion case, characterized by a μ -independent pitch-angle scattering frequency in Eq. (17). By contrast, it should be slightly more pronounced in the Kolmogorov turbulence, in which the equivalent of our χ -variable would scale with μ as $\chi = \mu^{1/3}$ rather than $\chi = \mu^{1/2}$. We conclude that the I-K turbulence confirmed by the rigidity spectrum must also manifest itself in a sharp in-

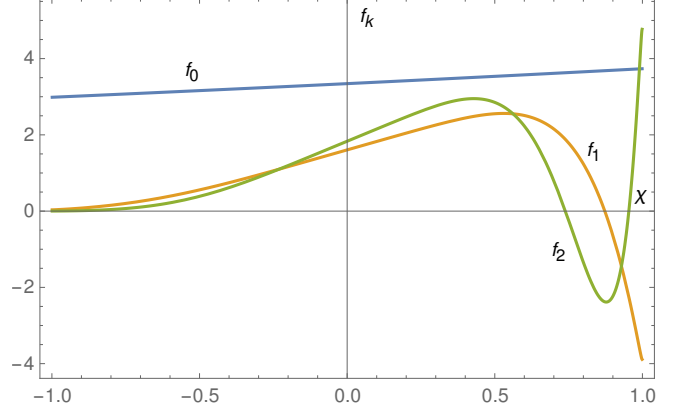


Figure 6. First three eigenfunctions $f_n(\chi)$, $n = 0, 1, 2$, of the spectral problem in Eq. (D21) for $\nu_\perp = 0.01$. They correspond to the three positive eigenvalues $\lambda_0 \approx 2\sqrt{5\nu_\perp} \approx 0.45$, $\lambda_1 \approx 45.0$, $\lambda_2 \approx 132$.

crease of the CR intensity across the magnetic horizon. The increase is predicted to have the following angular dependence:

$$f_0 \approx \sqrt{5/\lambda_0} \left[1 + \frac{\lambda_0}{4} |\mu|^{1/2} \text{sgn}(\mu) \right]. \quad (22)$$

Remarkably, a sharp increase across the presumed magnetic horizon ($\mu = 0$) in the CR intensity map was indeed observed by the HAWC and IceCube instruments. The best fit borderline between the global CR excess and deficit areas on the intensity map (black crossed curve in Fig. 11 of [Abeysekara et al. 2019](#)) does not seem to deviate from $\mu = 0$ line (black curve) by more than several degrees anywhere on the sky. This borderline position is predicted by Eq. (22), including the intensity profile across it, shown in Fig. 8 of the same reference. It shows a slice of the intensity map along the declination $\delta \approx -20^\circ$. The angular dependence in Eq. (22) can be recognized on the plot as a steep rise of the CR intensity near the RA angle $\Theta \approx \Theta_0 = 150^\circ$. Note that it is sufficient to replace our variable μ in Eq. (22) by $\mu \approx \pi(\Theta - \Theta_0)/180$ for this consideration.

However, the excess region spills over the magnetic horizon in some areas in the Northern Hemisphere, for example, at the Milagro Region B. Nevertheless, the spillovers are not in conflict with Eq. (22) since the latter represents only a gyro-tropic (gyro-phase averaged) component of the full angular distribution of CRs. The non-gyro-tropic correction to it can be significant due to, e.g., a nonlinear gyrophase bunching that occurs when particle gyromotion falls in resonance with a strong Alfvén wave (e.g., [Lutomirski & Sudan 1966](#); [Malkov 1998](#)). Unlike the robust sharp increase across the $\mu = 0$ line, the gyrophase bunching is likely to be transient. It may change due to the wave propagation or spreading of the particle bunch over the pitch-angle-gyrophase plane. Such spreading occurs due to the nonlinearity of oscillations of particles trapped into the resonance, augmented with other wave harmonics. However heuristic the above arguments,

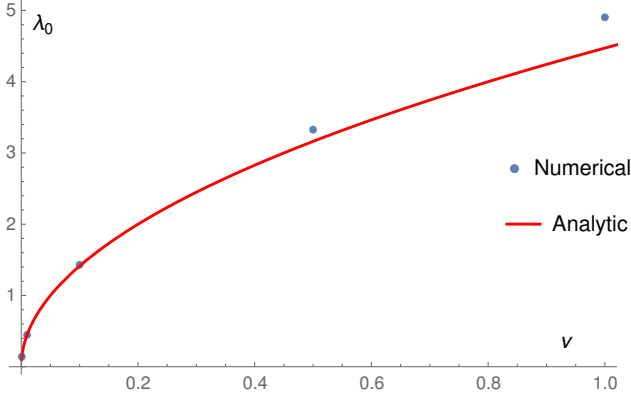


Figure 7. The “ground state” eigenvalue λ_0 as a function ν_\perp given in Eq. (21) (line) and direct numerical integration of Eq. (D21) (points).

the former Milagro Region B now looks quite different on the Milagro successors HAWC and IceCube’s intensity maps.

The energy dependence of the CR anisotropy must also be affected by a nearby source. Fig. 5 in [Amenomori et al. \(2017\)](#) shows an enhanced anisotropy in a limited range between 0.1 TeV and 100 TeV. It is this range where the spectral anomaly studied in this paper was observed. After the enhancement, the anisotropy briefly declines at ~ 100 TV, and then it starts growing again. We note that CRs reaccelerated at a nearby shock would merge into the background below this rigidity.

Meanwhile, the overall rigidity dependence of the CR anisotropy, considered in an extended range from 0.1–1000 TV, was interpreted as being approximately flat (e.g., [Cowsik & Madziwa-Nussinov 2016](#)). However, the flatness is inconsistent with the expected density gradient of CRs in the Galaxy combined with the rigidity dependence of their scattering rate (e.g., [Giacinti et al. 2018](#)). Hence, the anisotropy of Galactic CRs must grow with rigidity, as the pitch-angle scattering rate generally decreases with it.

Our model resolves the paradox of flat anisotropy. It is sufficient to subtract the contribution of CRs in the 10-TeV bump area, reaccelerated at a nearby source, and the CR anisotropy will grow with rigidity, as expected. An interesting question is how exactly it grows. Although the CRs reaccelerated nearby are more anisotropic than the background CRs, we can remove them from the data set by their rigidity range. We then take a somewhat broader range from the data in Fig. 5 of [Amenomori et al. \(2017\)](#) that show the anisotropy increase from $\sim 10^{-4}$ to 10^{-2} between 10^{-1} and 10^3 TV. This interval contains the bump. The critical point is that the background CRs propagate their final 3–5 pc through the same flux tube as the reaccelerated CRs. According to our model, they are also scattered by the I-K turbulence. Assuming then that the residual background CR anisotropy grows as R^δ , we indeed recover the I-K index $\delta \simeq 0.5$ from the above anisotropy data. This is the third independent indication of the I-K turbulence in the flux tube, in addition to the

theoretical consideration in Appendix B and the rigidity data fit in Sect. 5.

Another interesting signature of the I-K turbulence is a sharp variation of the CR intensity across the magnetic horizon. According to Eq. (22), the relative anisotropy of the CR intensity, I , near the magnetic horizon at $\Theta = \Theta_0$ can be represented as follows

$$\frac{I - \bar{I}}{\bar{I}} = \frac{1}{12} (\pi \nu_\perp |\Theta - \Theta_0|)^{1/2} \text{sgn}(\Theta - \Theta_0),$$

where \bar{I} is the all-sky average, the angle Θ is given in degrees, and the value of Θ is assumed to be close to Θ_0 . Unlike the rigidity fit obtained earlier, the above formula requires the fitting parameter ν_\perp that we cannot determine “from the first principles” at this point. However, the characteristic square root profile is recognizable in Fig. 8 of the paper by [Abeysekara et al. \(2019\)](#).

At the outset of this section, we emphasized the role of a nearby star magnetically connected with the heliosphere. If a better candidate is not found, the Epsilon Eridani will likely be the first object on the sky directly linked to a significant part of the Galactic CR spectrum in the relevant energy range between ~ 1 TeV and 100 TeV.

8. TOPOLOGY OF THE MAGNETIC FIELD IN THE SOLAR NEIGHBORHOOD

It is clear that the structure of the local magnetic field may facilitate CR transport from one direction and impede it from another. To ascertain how stringent the magnetic connectivity requirement is, we extend the discussion of the Local Bubble in Sect. 2 by zooming into several pc around the Sun.

Both the matter distribution and magnetic topology in solar proximity are challenging to describe. Most of the objects (other stars, pulsars, and quasars) suitable to probe the medium within 3–10 pc of the Sun are located too far away, and thus any such probe has to be corrected for the properties of the medium along the line of sight. Nevertheless, much has been learned over the recent decade, although there are two somewhat different views on the local environment. Each of them might impact our model in different ways. Therefore, we are discussing them separately.

8.1. Complex Local Interstellar Clouds (CLIC)

The CLIC model describes the local ISM environment as a cluster of isolated clouds ([Redfield & Linsky 2008](#); [Frisch et al. 2011](#); [Linsky et al. 2019](#)). Using 157 stars within 100 pc around the Sun, [Redfield & Linsky \(2008\)](#) were able to identify 15 partially ionized WIM clouds with temperatures ranging between 3900 K and 9900 K. These clouds fill a volume within 15 pc of the Sun. According to these studies, four such clouds are currently interacting with the heliosphere ([Linsky et al. 2019](#)). More precisely, the Sun is currently located at the very edge of the Local Interstellar Cloud (LIC) and will leave it in 3000 years, if not earlier, transiting to the G Cloud. This region has a higher temperature and lower gas density than the WIM. While the inter-cloud gas temperature turned

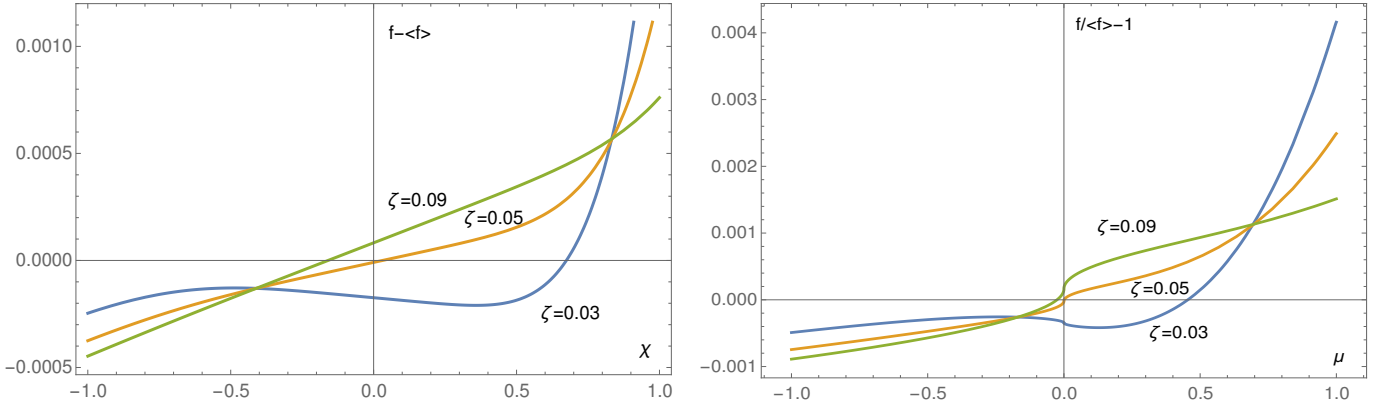


Figure 8. Left panel: particle angular distribution $f - \langle f \rangle$, using variable χ that shows no enhanced anisotropy at $\chi = 0$. Right panel: the same three solutions as a function of μ shown as a relative anisotropy, $(f - \langle f \rangle) / \langle f \rangle$. The isotropic part $\langle f \rangle \approx 0.50$ for all three values of ζ , and decreases with ζ insignificantly, since $\nu_{\perp} = 10^{-6}$ and $\lambda_0 \approx 0.00447$, $\lambda_1 \approx 45.0$, $\lambda_2 \approx 132$. The source anisotropy is $Q_1(\chi) = 1 + 0.01|\chi|^3$. See Eq. (18) for dimensionless redefinitions of f and ζ .

out to be lower than 10^6 K (earlier estimates), it remains ionized, due to, e.g., past supernova events (Breitschwerdt & Schmutzler 1999).

The local magnetic field direction, poorly known a decade ago, is now measured using independent techniques producing consistent results (Zirnstein et al. 2016). However, given the complexity of matter distribution under the CLIC concept, the local field direction probably does not persist across the CLIC. It shall then be naive to determine whether a nearby star is magnetically connected with the Sun by extending the local field line. The relative cloud motion perturbs the large-scale magnetic field in the inter-cloud space next to the Sun. Since the inter-cloud field is frozen into the hot plasma, not mixing with the cloud gas, the field is likely to align with the adjacent cloud boundaries. The results of the Solar Wind ANisotropies (SWAN) experiment on board the Solar and Heliospheric Observatory (SOHO) satellite and the Interstellar Boundary EXplorer (IBEX) point to the same direction of the magnetic field just outside of the heliosphere, i.e. it is roughly tangent to the boundary of the Local Cloud in the direction of the G-cloud, as expected if field lines are compressed between both clouds (Ferrière 2015). The heliosphere perturbs the local field by draping the ISM magnetic field and the solar wind outflow (so-called Axford-Cranfill effect, Axford 1972).

Therefore, the star responsible for the bump is not required to have its angular coordinates tightly aligned with the local field direction because extraneous cloud motions bend the CR flux tube. The latter makes its way to the Sun between the clouds. In this case, our task is to ascertain whether, given star coordinates and the local field direction, the field can change its direction in the local ISM to connect to the star. To this end, we will consider both the sharp local changes in the field direction, e.g., caused by perturbations of the ISM by the heliosphere itself and gradual ones associated with the motions of isolated clouds and turbulence.

The flux tube may also twist and bend intrinsically. Since the CRs reaccelerated at a bow shock are mostly protons,

they will carry a current along the flux tube that needs to be compensated by the plasma return current to maintain the medium's charge neutrality. This current may drive a kink instability that will bend and twist the flux tube. Rough requirements for its onset come from the classical Kruskal-Shafranov (K-S) threshold. It is usually expressed in terms of a critical current flowing through a plasma column, $I_{KS} = \pi l_{\perp}^2 c B / L$, where l_{\perp} is the radius of the plasma column and L – its length. The plasma column here is floating between two conducting electrodes.

More analogous to the CR flux tube is a plasma column insulated from anode and its respective end can move freely (Furno et al. 2006; Ryutov et al. 2006), similar to that in a well-known plasma lamp (aka Tesla ball). This setting would substantially decrease the instability threshold. Let us rewrite the conventional K-S threshold in terms of a number density of reaccelerated CRs:

$$\frac{n_{CR}}{n_0} > 4\pi \frac{V_A^2}{cu} \frac{r_{GV}}{\zeta}. \quad (23)$$

Here n_0 is the background plasma density, V_A is the Alfvén velocity, $u = U_{sh} / \cos \Theta_{nB}$ (with U_{sh} and Θ_{nB} being the shock velocity and the obliquity angle, respectively), and r_{GV} is the Larmor radius of a GV proton. For an estimate, we have replaced the plasma column length L in the K-S threshold with a local distance from the shock, ζ . Indeed, $n_{CR}(\zeta)$ decreases along the tube from its maximum at the shock, $n_{CR}(0)$, that exceeds the background CR density by the factor $K \approx 2.4$, according to the fit in Sect. 5. Assuming the inter-cloud density $n_0 \lesssim 0.01$ (Linsky et al. 2019), we estimate $n_{CR}(0)/n_0 \sim 10^{-6}$. The l.h.s. of Eq. (23) decreases with ζ faster than its r.h.s. The $n_{CR}(\zeta)$ can be estimated from Eq. (5) assuming an I-K turbulence spectrum and the power-law index of CR, $q \approx 4.5$, for simplicity. This yields a simple scaling $n_{CR} \propto l_{\perp}^3 / \zeta^3$, so that we obtain the effective length of the kink-unstable part of the flux tube,

$$\frac{L_{unst}}{l_{\perp}} \sim \left(\frac{l_{\perp}}{r_{GV}} \frac{n_{CR}(0)}{n_0} \frac{cu}{V_A^2} \right)^{1/2}. \quad (24)$$

Given the parameters estimated above, we find $L_{\text{unst}}/l_{\perp} \gtrsim 10$ being perhaps insufficient to dislocate the source's magnetic coordinates by more than a few degrees for $l_{\perp} \sim 10^{16}$ cm. However, the above L_{unst} gives only a conservative lower bound to this quantity. First, the Kruskal-Shafranov threshold is significantly lower in the case of a plasma column with a “loose end,” as we already mentioned. Second, we estimated $n_{\text{CR}}(0)$ from the fit in Sect. 3, neglecting lateral losses from the tube, which is unrealistic. Given $\zeta_{\text{obs}} \gg l_{\perp}$, the losses must be very significant. We note that the fit remains accurate since changes in $n_{\text{CR}}(0)$ are compensated by changes in the shock compression ratio, Sect. 5. The reason is that the fit contains a combination of these parameters, entering the spectrum normalization parameter $K \approx 2.4$, which in reality is higher at the base of the flux tube due to the neglected losses.

The magnetic connectivity criterion may promote the Epsilon Eridani star to the leading candidate for the CR bump as this star is close to the local field direction. Its Galactic J2000 coordinates³ are $(l_{\text{Eri}}, b_{\text{Eri}}) = (196^\circ, -48^\circ)$, while the local field direction at >1000 au from the Sun is evaluated by Zirnstein et al. (2016) based on IBEX data: $(l_{B_{\text{loc}}}, b_{B_{\text{loc}}}) = (206^\circ, -50^\circ)$. Here we converted their coordinates $(l'_{B_{\text{loc}}}, b'_{B_{\text{loc}}}) = (25.98^\circ \pm 0.70^\circ, 50.09^\circ \pm 0.57^\circ)$ using an expression:

$$(l_{B_{\text{loc}}}, b_{B_{\text{loc}}}) = (l'_{B_{\text{loc}}} + 180^\circ, -b'_{B_{\text{loc}}}). \quad (25)$$

The kink instability of the flux tube discussed above can compensate for the difference between the direction of the magnetic field and the location of the star. Note also a huge size of the astrosphere of Epsilon Eridani that is approaching 1° and an even larger bow shock it creates. More importantly, for other passing star candidates, such as Epsilon Indi, the local field direction is unlikely to persist beyond a distance comparable to the size of local clouds in the CLIC, as we stated earlier. Since the heliosphere is believed to be practically in the inter-cloud space, the local field most probably aligns with the cloud boundary.

The next set of data about the field direction concerns a larger volume around the Sun, about 40 pc across. The field orientation is determined here with a significantly lesser accuracy than locally. Ferrière (2015) summarizes the results of Lallement et al. (2005) as $(l_{B_{40}}, b_{B_{40}}) = (227^\circ \pm 20^\circ, -25^\circ \pm 20^\circ)$, with the errors being only roughly estimated. A more recent systematic study by Frisch et al. (2015) provides $(l_{\text{F}}, b_{\text{F}}) = (206^\circ, -49^\circ)$ with a somewhat lesser uncertainty $\pm 16^\circ$. (Note that these magnetic field directions are also converted using Eq. [25].) This direction is consistent with the local direction discussed in the previous paragraph but, given the significant uncertainty, may be distinct from it. The difference is expected since, in addition to the field perturbations caused by the local clouds, the scales of energy injection into the ISM turbulence are likely to include the 1–5

pc interval (Haverkorn et al. 2008). The above data constitute an average field direction that may fluctuate on this scale, which is just in the range of distances to the stars we are interested in. Minimal fluctuation would place Epsilon Eridani on the same magnetic line with the Sun since the field direction indicated above is only $\approx 6.7^\circ$ away from the star's position on the plane of the sky. Alternatively, curvature and diamagnetic drifts, as well as a lateral spreading of CRs, can compensate for this minor mismatch.

While the Epsilon Eridani star can seamlessly align with the local (and the 40-pc averaged) field, the Epsilon Indi requires a significant field line deflection from the local direction to connect the reaccelerated CRs to the Sun. The Epsilon Indi star has Galactic coordinates³ $(l_{\text{Ind}}, b_{\text{Ind}}) = (336^\circ, -48^\circ)$, that is, $\approx 70^\circ$ away from the local field direction. In part, the deflection might occur locally due to the heliospheric distortion of the ISM field mentioned earlier (see the previous paragraph, as well). However, additional gradual deflection by as much as $\sim 90^\circ$ over the 3.6 pc distance between the Sun and the star might be necessary. It does not seem to be impossible if the field is largely wired through the inter-cloud space, especially with some assistance from the kink instability. We conclude that the magnetic connection with the Epsilon Eridani star is practically guaranteed if the field maintains its local direction over a distance ~ 3 pc. The connection to other possible sources that are not aligned with the local field is strongly affected by the CLIC cloudlets.

8.2. Single Cloud Morphology

An alternative account of the ISM within ~ 10 pc of the Sun is proposed by Gry & Jenkins (2014, 2017). In their interpretation of the UV absorption data, the heliosphere is located inside of a single monolithic cloud. Its bulk velocity is perturbed at different locations so that the sightline velocities are perceived as coming from independently moving clouds. Gry & Jenkins (2014) provide two motivations for the revision of the Redfield & Linsky (2008) model, outlined above. First, for isolated clouds, one would expect some sightlines to pass between them, which was not observed. This objection does not seem to be crucial, given the limited number of sightlines and uncertain filling factor of the clouds. The second objection regards the lack of evidence in the Ca-II K data to support the G Cloud existence (Crawford et al. 1998). However, this objection does not logically rule out other clouds as separate entities, with a hot ionized medium between them. The Gry & Jenkins (2014) model has the advantage of a fewer number of free parameters, but the Redfield & Linsky (2008) model fits the data more accurately. The mono-cloud configuration might have a strong impact on the Epsilon Indi scenario and would probably be less important for the Epsilon Eridani scenario, since its direction is close to the local field.

8.3. Implications for Cosmic Rays

While not making a definitive selection between the two morphologies, we slightly incline to the Redfield & Linsky (2008) model, as it implicates a sizable volume of highly

³ <http://simbad.u-strasbg.fr/simbad>

ionized inter-cloud plasma through which the CR flux tube with self-generated turbulence can be channeled. Switching to the Gry & Jenkins (2014) concept would require a reconsideration of the CR propagation through the WIM. However, one aspect of the Gry & Jenkins (2014) interpretation of the data might have important implications for our CR reacceleration model. Namely, they infer from the data a shock wave slowly moving through the Local Cloud towards the heliosphere. They further hypothesize that this is an imploding shock caused by a pressure imbalance between the Local Cloud and a hot Local Bubble plasma. While the shock is subsonic, it might be in a radiative state, thus having a significant compression ratio ~ 1.5 , despite a relatively low speed of $20\text{--}26\text{ km s}^{-1}$. These shock parameters are not very promising for efficient CR acceleration. However, if the shock is quasi-perpendicular, as suggested, it may accelerate more efficiently operating in a shock-drift acceleration regime.

The single cloud scenario, suggested by Gry & Jenkins (2014), has an advantage for our reacceleration model of not being constrained by magnetic connectivity requirement since the proposed imploding shock should cover half of the sky. We also note that its effect on the possible time variability of the CR bump might be the opposite of a nearby bow shock. Although the observer is still upstream of the shock, we do not expect a strong suppression of particle diffusivity associated with the flux tube crossing discussed in Sect. 5. In this case, the lower-energy break (hardening) will likely decrease with time, as particles with progressively lower energies can diffuse to the observer from the shock, Eq. (5).

9. MODEL SUMMARY

We have proposed an astrophysical explanation of the excess in the Galactic CR proton spectrum, recently observed with an unprecedented accuracy. The key elements of our model are as follows:

1. The unexpected bump in the 10 TV rigidity range is entirely a product of reacceleration of the pre-existing CRs in the Local Bubble (both primary and secondary) by a weak shock wave, such as a bow shock of a passing star or an imploding shock moving through the Local Cloud. We exclude a source of primary freshly accelerated CRs, such as a nearby SN remnant (SNR), as the main contributor to the bump, because of the co-presence of secondaries in it which cannot be “fresh”.
2. In the current epoch, the bow shock is magnetically connected with the Sun. The reaccelerated CRs reaching the Sun propagate through a magnetic flux tube with an enhanced scattering turbulence generated by these CRs. It is primarily driven by CR pressure gradient across the flux tube. A turbulent cascade to shorter scales maintains the I-K Alfvén wave spectrum, $\propto k^{-3/2}$. It leads to the particle mean-free path that scales as $\lambda \propto \sqrt{l_{\perp} r_g}$ with the flux tube characteristic scale l_{\perp} and particle gyroradius r_g . This scaling is robust, as it is required to fit the entire rigidity pro-

file of the bump with correct amounts of hardening and softening.

3. Propagation through the I-K turbulent flux tube leaves imprints in the CR arrival directions. The intensity map has a narrow excess near the magnetic field direction for particles coming from the source and a shallow deficit in the opposite field direction. It also has a sharp increase across the magnetic horizon. These model predictions are qualitatively consistent with observations.

We have solved the model equations, initially using the unknown shock Mach number, M , and the nominal distance from the shock to the Sun, ζ_{obs} , as fitting parameters. We have fitted the solution to the most recent data including the TeV CR excess with a $\sim 0.1\%$ accuracy. Capturing the complexity of the CR excess requires six ad hoc parameters. These are the two break rigidities, two widths of the breaks, and two changes of the spectral index at the breaks. Our model solution is determined by only *two physical quantities*. These are the Mach number M and the bump rigidity R_0 , whereas R_0 depends on the distance to the shock and its size. This significant reduction in the number of fitting parameters makes a coincidental agreement highly unlikely. As the model has no free parameters, we were able to constrain unknown physical parameters. Our findings are:

1. The distance to the bow shock along the flux tube $\zeta_{\text{obs}} = 3\text{--}10\text{ pc}$, assuming that the characteristic scale of the flux tube (bow shock) across the field is $l_{\perp} \sim 10^{15} - 10^{16}\text{ cm}$.
2. The characteristic sound Mach number on the part of the shock that efficiently reaccelerates CRs is $M \approx 1.5\text{--}1.6$.

The scales are obtained assuming that the shock is propagating in a hot ISM with the temperature $T \sim 10^6\text{ K}$, which for the calculated Mach number corresponds to the shock speed $u \sim 100\text{ km s}^{-1}$. Our model parameters are summarized in Table 1.

10. DISCUSSION AND OUTLOOK

It is, perhaps, too early to embark on quantitative modeling of the secondaries Li, Be, B, as well as on heavier primaries, He, C, and O. In the relevant rigidity range $\gtrsim 200\text{ GV}$ they still have significant error bars (Ahn et al. 2008; Aguilar et al. 2017, 2018a). However, it is clear that the spectral hardening above $\gtrsim 200\text{ GV}$ is more pronounced in the spectra of secondaries. One can roughly reproduce this difference through the injection of pre-existing CR species to the shock solution and limiting their acceleration in the region above the spectral hardening because of the shock weakness. While the resulting softening of the overall primary spectrum is not pertinent to the reaccelerated secondaries, the latter will have a stronger break than the primaries.

Worth mentioning is that the proposed scenario of the local magnetosonic or bow shock predicts the same rigidity for the

spectral breaks for all CR species. Though very different in underlying physics, the implications are similar to the “propagation scenario” (Vladimirov et al. 2012) mentioned in the introduction and require very few free parameters. However, instead of the “propagation scenario” pertinent to the whole Galaxy, our proposed scenario is local. Observations of the diffuse emission above ~ 30 GeV from the interstellar gas at different distances from the Sun may be able to discriminate between several scenarios of the observed bump, such as the local disturbance or the global properties of the ISM.

We found, at least, two closeby fast-moving stars that may drive shocks capable of CR reacceleration, the double Scholtz’s star and triple Epsilon Indi, and a slower star, Epsilon Eridani, that has a mass loss rate of $30\dot{M}_\odot$ and a huge astrosphere extending over $42'$ on the sky. Our model is directly applicable to both the Epsilon Indi and Epsilon Eridani systems. The former should have a bow shock that is very much different from the shock formed by a single star. There is also a possibility of 11-yr variations in the CR bump properties due to the 11-yr orbital period of its widely separated A and B+C components. The latter, Epsilon Eridani, is the closest of the three and is aligned with the direction of the local magnetic field that makes it a primary candidate. The turbulence left behind the double Scholtz’s Star, which is moving away from the Sun, may also provide an enhanced scattering and confinement of particles at the rigidities beyond the TV range.

Another possibility is a weak imploding shock moving through the Local Cloud or a magnetosonic shock propagating through the rarefied plasma in the Local Bubble. In ordinary gas dynamics an arbitrary initial motion generally steepens into shocks, unless dissipative effects come into play ear-

lier (Whitham 2011). In the collisionless plasma of the Local Bubble wave dispersion and ion reflection off the shock front may damp the shock by enabling anomalous (i.e. collisionless) dissipation mechanisms (Sagdeev 1966). However, for this to happen the shock needs to be supercritical (Kennel 1988), i.e., typically having the Mach number $M \gtrsim 2$. This is not the case for the shock of $M \approx 1.5$ – 1.6 that we inferred by fitting the observed spectrum. We conclude that such shocks may propagate in the Local Bubble even long after the last SN explosions we discussed in Sect. 2. Other sustainable sources of mechanical energy capable of driving weak shocks have also been suggested (e.g., Cox & Helenius 2003).

Additional support to the local origin of the TV bump comes from its enhanced anisotropy associated with the source proximity. The background CR anisotropy is then much lower in the TV range. However, with the bump-CRs added, the total observed anisotropy appears as an almost flat function of rigidity, as observed. The angular structure predicted by the model contains a robust step-like feature near the magnetic horizon, which also has been detected by HAWC and IceCube. We defer the quantitative comparison of the anisotropic component of the model with the data to a separate study.

ACKNOWLEDGMENTS

We thank the anonymous referee for useful comments. Mikhail A. Malkov acknowledges support from NASA ATP-program within grant 80NSSC17K0255 and from the National Science Foundation under grant No. NSF PHY-1748958. Igor V. Moskalenko acknowledges support from NASA Grant No. NNX17AB48G.

APPENDIX

A. WAVE GENERATION

Although macroscopic in nature, Eq. (8) approximately applies to the partial CR pressure, $P_{\text{CR}}(R)$, and wave spectral energy, $E_w(k)$, if the particle distribution is nearly isotropic. In this case, a simplified resonance condition for the wave-particle interaction, $k \approx r_g^{-1}(R)$, may be adopted instead of the more accurate cyclotron resonance condition, $k_{\parallel} v_{\parallel} \approx \omega_c(R)$ (Skilling 1975). The partial pressure of reaccelerated CRs and the wave energy density in Eq. (8) are normalized as follows

$$P_{\text{CR}}(p) = \frac{8\pi c}{3\rho V_A^2} p^4 (f - f_\infty),$$

$$\frac{\langle \delta B^2 \rangle}{B_0^2} = \int E_w(R) d(\ln R).$$

Since we already know the CR enhancement from the fitting parameter K , we can quantify their suppression effect on κ , as compared to its large background value, $\kappa_{\text{ISM}} \sim 10^{28} \text{ cm s}^{-1}$ (for GV particles).

Being controlled by the wave generation, the suppression factor is limited by a nonlinear saturation, cascading, and damping of the self-generated waves. These phenomena are not included in Eq. (8). A plausible expectation is that the waves saturate at $\delta B \sim B$ for $k \sim r_g^{-1}$ under a sufficient pressure gradient ($f \gg f_\infty$) that drives these waves (McKenzie & Voelk 1982; Völk et al. 1984). The diffusion coefficient of the resonant particles is then close to the Bohm value⁴, $\kappa_B = cr_g/3$. However, unlike the CRs that are freshly accelerated at strong shocks, the pressure of reaccelerated CRs only moderately exceeds the background CR pressure (by a factor of $K \approx 2.4$).

We, therefore, determine κ_{\parallel} using a quasi-linear approximation, according to which it remains reasonably large com-

⁴ Shorter waves may saturate at higher amplitudes, $\delta B \gg B_0$ (Bell 2004), close to strong shocks, but their impact on the particle confinement may even be negative. Indeed, $\kappa(R)$ grows too steeply with R , $\kappa \propto R^2$, when these short waves dominate the spectrum. Besides, the shock is weak in our case.

pared to κ_B , but much smaller than the background value κ_{ISM} . As the amplitude of the waves decreases outside of the shock precursor, κ_{\parallel} increases and approaches an intermediate value κ_{int} , such as $\kappa_B \ll \kappa_{\text{int}} \ll \kappa_{\text{ISM}}$. This value is typical for such distances from the shock where an enhanced turbulence generated by the reaccelerated CRs persists while the CRs begin to escape the shock surroundings along the field, albeit with the suppressed particle diffusivity. Their diffusion is impeded by self-generated waves that propagate at a low speed, V_A . Hence, an enhanced turbulence persists even after the CRs largely diffuse away. We incorporate this effect into the integration constant of Eq. (8). The quasilinear result then reads

$$\kappa_{\parallel} = \frac{\kappa_B}{E_w} = \left(1 + \frac{u}{V_A}\right) \frac{\kappa_B}{P_{\text{CR}} + P_{\text{int}}}, \quad (\text{A1})$$

where we have defined an arbitrary constant $P_{\text{int}} = (\kappa_B/\kappa_{\text{int}})(1 + u/V_A)$ that comes from the integration of Eq. (8). It satisfies the boundary condition $\kappa_{\parallel} \rightarrow \kappa_{\text{int}}$ for $P_{\text{CR}} \rightarrow 0$, and represents the diffusivity suppression ahead of the shock at $\zeta \sim \zeta_{\text{int}}$, where the reaccelerated particles diffuse away, but the wave turbulence is still significant, $\kappa_{\text{int}} \ll \kappa_{\text{ISM}}$.

To find P_{CR} , we close Eq. (8) by a convection-diffusion balance for P_{CR} along the flux tube,

$$uP_{\text{CR}} + \kappa_{\parallel} \frac{\partial P_{\text{CR}}}{\partial \zeta} = 0. \quad (\text{A2})$$

This balance extends Eq. (1) to the area further ahead of the shock precursor by applying it along the flux tube.

Near the shock the particle transport turns towards the shock normal, as $\kappa_{\perp} \approx \kappa_B^2/\kappa_{\parallel}$ increases. This part of the precursor does not contribute significantly (see Sect. 3) to the path integral in Eq. (6). We place it after the main part on the r.h.s. of the result below. From Eq. (6), using (A2), we thus obtain:

$$\begin{aligned} \Phi(R, \zeta_{\text{obs}}) &= \ln \frac{P_{\text{CR}}(0)}{P_{\text{CR}}(\zeta_{\text{obs}})} \\ &\simeq \frac{u\zeta_{\text{obs}}}{\kappa_{\text{int}}} + \ln \left[P_{\text{CR}}(0) \frac{\kappa_{\text{int}}}{\kappa_B} \left(1 + \frac{u}{V_A}\right)^{-1} \right]. \end{aligned} \quad (\text{A3})$$

Here we have also assumed that $\zeta_{\text{obs}} \gg \zeta_{\text{int}}$. To be consistent with the fit, this expression must vary with R as $R^{-1/2}$, according to Eq. (10). Assuming then that $\kappa_{\text{int}} \propto R^{1/2}$, which we will justify in Appendix B, we find that only the first term on the r.h.s. behaves this way. The second term varies as $\ln R$. Besides, it does not contribute to the range of $\Phi(R)$ significantly. Indeed, according to the fit in Sect. 5, Φ varies by a factor ~ 100 in the interval $30 \text{ GV} < R < 100 \text{ TV}$ which is well above the range of the second term on the r.h.s. of Eq. (A4). It varies by less than an order of magnitude in the same rigidity range.

The main contribution to Φ thus comes from an extended region outside of the shock precursor, which gives us an access to the distance to the source. Unlike the second term,

this contribution is directly proportional to ζ_{obs} . However, this is a quasilinear result that needs to be modified if the wave-wave interaction, not included in Eq. (8), is essential. The other obstacle to the estimate of ζ_{obs} is the unknown κ_{int} . We will also consider these aspects in Appendix B.

It follows that a cloud of reaccelerated CRs must be self-confined in the lateral and wake areas of the bow-shock before they escape the star surroundings. The CR cloud must also be elongated in the field direction, because $\kappa_{\perp} \approx \kappa_B^2/\kappa_{\parallel} \ll \kappa_{\parallel}$. Since the CR pressure gradient is then directed largely across the field, the resonant cyclotron and the nonresonant CR current, or Bell (2004) instabilities that develop most rapidly along the field are less efficient than the CR pressure-driven acoustic instability. The latter, also called Drury instability (Dorfi 1984; Drury & Falle 1986; Kang et al. 1992), has been compared with the nonresonant instability by Malkov et al. (2010b).

Although only a specific case of CR modified shock precursor has been considered in the comparison, in which both the CR current and pressure gradient instabilities stem from the same CR population balanced by the ram pressure of the inflowing plasma, we can apply some of those results to the present study. For the plasma- $\beta \sim 1$, the growth rates of Drury and Bell instabilities are similar, even assuming the Bell instability operating under the most favorable conditions of the field aligned current and wave vector. Drury instability, however, is not sensitive to its wave vector orientation with respect to the field, particularly if $\beta > 1$, which is likely to be the case in the Local Bubble (Spangler 2009). Therefore, Drury instability should drive waves across the field more efficiently.

Now we focus on the saturated spectrum of this instability and its implications for the CR scattering. Unlike in the resonant cyclotron and Bell instabilities the magnetic perturbations of the acoustic instability can be considered as passively frozen into the fluid perturbations. Assuming that $\beta > 1$, this approximation is sufficient for our purposes. Later we will take magnetic perturbations pertaining to the particle scattering into account. First, we adopt a reduced equation for unidirectional acoustic perturbations driven by the CR pressure gradient in the form presented by Malkov & Diamond (2009). In a CR cloud elongated along the field line in ζ -direction, the CR pressure is in r -direction, in a cylindrical symmetry, for example. We neglect ζ -dependence for now, also considering r as a locally Cartesian coordinate. The equation for unstable acoustic waves can be written as a 1-D evolution equation:

$$\frac{\partial \tilde{\rho}}{\partial t} - C_s \frac{\partial \tilde{\rho}}{\partial r} - \frac{\gamma + 1}{2\rho_0} C_s \tilde{\rho} \frac{\partial \tilde{\rho}}{\partial r} - \mu \frac{\partial^2 \tilde{\rho}}{\partial r^2} = \gamma_D \tilde{\rho}, \quad (\text{A4})$$

where C_s is the sound velocity, $\tilde{\rho}$ is the plasma density perturbation, ρ_0 is its background density, and γ is the adiabatic index. The l.h.s. is essentially a Burgers equation that describes unstable waves (driven by the instability term on the r.h.s.) aligned with the CR gradient and propagating along the characteristics $r = -C_s t + r_0$. The characteris-

tics $r = C_s t + r_0$, associated with the damped waves, have already been eliminated from Eq. (A4).

The small viscosity μ is only important at discontinuities, resulting from the nonlinear steepening of unstable waves. The growth rate for these waves is

$$\gamma_D = -\frac{1}{2\rho_0 C_s} \frac{\partial \bar{P}_{\text{CR}}}{\partial r}, \quad (\text{A5})$$

where \bar{P}_{CR} is the full (momentum integrated) CR pressure. The growth rate has also a stabilizing component owing to the CR diffusion. We have omitted it since it is small compared to γ_D , assuming that $\kappa/l_\perp > C_s$. Here l_\perp is the characteristic scale of the pressure gradient ($l_\perp^{-1} \sim \bar{P}_{\text{CR}}^{-1} \partial \bar{P}_{\text{CR}} / \partial r$).

A handle on the dynamics and saturated state of the unstably driven Burgers turbulence can be obtained by transforming to the reference frame moving with unstable sound waves, $r \rightarrow r + C_s t$. This boost along r transforms away the second term on the l.h.s. of Eq. (A4). Small-amplitude seed waves will then grow exponentially until the third (nonlinear) term balances the driver on the r.h.s. Before it happens, the initial, say sinusoidal, profile of the seed perturbation steepens into a periodic shock sequence with the seed wave period. In this saturated state, the following balance is maintained across the most part of the period:

$$\frac{\partial \tilde{\rho}}{\partial r} \approx \frac{1}{(\gamma + 1) C_s^2} \frac{\partial \bar{P}_{\text{CR}}}{\partial r}. \quad (\text{A6})$$

As the viscous term in Eq. (A4) remains small everywhere except in the shock transition, the density $\tilde{\rho}$ has a saw-tooth profile. It consists of smooth curves with slopes proportional to the local slope of \bar{P}_{CR} , connected by the shocks. For this reason it is called a shock-train solution. The latter is a generic consequence of nonlinear and instability terms present in many evolution equations studied in the past (see, e.g., Malkov & Diamond 2009 and references therein).

The shock-train solution is in compliance with a natural requirement that the period averaged $\langle \tilde{\rho} \rangle \approx 0$, while, according to Eq. (A6) it must remain monotonic almost everywhere, except for the thin shock transitions. It also proved to be a strong attractor to which a broad class of initial profiles converge. Meanwhile, in the shock transitions the last term on the l.h.s. of Eq. (A4) is of the same order as the nonlinear and instability terms. The fact that the slope of $\tilde{\rho}$ between the shocks closely follows that of the \bar{P}_{CR} , immediately relates the amplitude of the density jumps to the distance between the shocks, a property that we will use in the sequel.

B. WAVE ENERGY TRANSFORMATION

Unlike in an idealized periodic solution discussed earlier, in any realistic shocktrain structure shocks have different strengths. Therefore, they move at different speeds and coalesce, so their strengths increase while fewer shocks remain in the system. However, this shock dynamics is typical for a one-dimensional system evolving, for example, in a periodic

box, with a time-asymptotic state of only one strong shock per period.

The system considered here has at least three important differences. First, unlike the initial value problem outlined in the previous subsection, the seed waves are continuously fed to the Drury instability from the resonance instability of CRs diffusing away from the bow shock. Hence, the asymptotic single-shock state of a maximum strength is unrealistic. Second, the shock formation occurs in an elongated region being two-dimensional, at a minimum. The shocks propagate then towards its axis at different, albeit close angles. Therefore, their coalescence proceeds along intersection lines, not along the entire shock surface simultaneously. As a result, a random web-like shock network emerges. Third, the inverse cascade associated with the shock merger events is arrested by the forward Alfvén cascade at a scale that plays a role of the Rhines's scale. This effect is akin to the Rhines's phenomenon where an inverse eddy cascade is intercepted by a wave turbulence cascade (Rhines 1975). We will discuss this scenario below for the sake of CR scattering by the Alfvén waves.

Let us first estimate the density of the shocks and their average strength while they merge. These quantities will determine the spectrum of Alfvén waves that are generated by the shock merger. The particle diffusivity along the field, κ_{int} , depends on the Alfvén spectrum. We recall that we need κ_{int} to derive the distance to the bow-shock using Eq. (6).

To describe the shock merger, we return for a while to the simple picture of a periodic 1-D shocktrain. Let its initial period be $2b$. The energy density of the shock train moving at a speed C_s , as in ordinary acoustic waves, has two quadratic contributions. They come from the density and velocity perturbations and are equal in a plane acoustic wave (Landau & Lifshitz 1987), thus carrying the specific energy density $C_s^2 \tilde{\rho}^2 / \rho_0^2$. Using Eq. (A6), we can write this quantity within one shocktrain period between the points $r = \pm b$, as

$$E = \frac{C_s^2}{2b\rho_0^2} \int_{-b}^b \tilde{\rho}^2 dr = \frac{b^2}{3(\gamma + 1)^2 \rho_0^2 C_s^2} \left[\frac{\partial \bar{P}_{\text{CR}}}{\partial r} \right]^2. \quad (\text{B7})$$

We have used an approximation of linear $\bar{P}_c(r)$ on a short interval $b \ll l_\perp$. Introducing the shocktrain amplitude parameter A ,

$$A^2 = \frac{2\pi^2}{3(\gamma + 1)^2 \rho_0^2 C_s^2} \left[\frac{\partial \bar{P}_{\text{CR}}}{\partial r} \right]^2,$$

and the shocktrain wave number $k_0 \equiv \pi/b$, we can express the above energy density through the spectral density as follows:

$$\frac{A^2}{2k_0^2} = \int_{k_0}^{\infty} E_k^s dk.$$

From here we obtain the shocktrain spectral density E_k^s :

$$E_k^s = \begin{cases} A^2 k^{-3}, & k \geq k_0; \\ 0, & k < k_0. \end{cases} \quad (\text{B8})$$

It is seen that as the shocks merge, that is k_0 decreases, the total energy density increases as k_0^{-2} . The spectrum at $k > k_0$ is unaffected by the mergers and remains *independent* of k_0 , as we consider the amplitude parameter A , that is the $\partial \bar{P}_{\text{CR}}/\partial r$ profile, to remain constant. This convenient feature of the acoustic inverse cascade allows us to evade a difficult question of how to determine k_0 for the purpose of obtaining a magnetic counterpart of the acoustic shocktrain turbulence. Since the inverse cascade proceeds to a sufficiently small value $k_0 \gtrsim l_\perp^{-1}$, we may assume that $k_0 r_{g,\text{max}} < 1$ and the longest waves will not influence the CR scattering significantly. As we know from the fit, the maximum rigidity of reaccelerated CRs is in the range 10 – 100 TV, so the gyroradius cannot significantly exceed 10^{16} cm in a few μG field. Further constraints on k_0 would require a consideration of the lateral profile of the CR flux tube, which is beyond the scope of this paper.

In the zeroth approximation, magnetic perturbations associated with the shocktrain generation passively follow the gas motion in acoustic waves. In the Local Bubble plasma, presumably with $\beta > 1$, oblique magnetosonic perturbations would be strongly damped, were they not be driven by the CR pressure gradient. In contrast to the driven magnetoacoustic waves, Alfvén waves generated by the shocktrain turbulence propagate along the field essentially undamped and cascade to shorter scales, thus interacting with all reaccelerated CRs. Alfvén wave generation is quite similar to what is known in the MHD turbulence studies as “Alfvénization” of the Kolmogorov hydrodynamic cascade. Although the excitation of waves with longer scales is also expected due to the helicity conservation, we focus on the direct Alfvén cascade as it is relevant to the CR scattering. It proceeds via interaction of counter-propagating Alfvén wave packets, as described by, e.g., Goldreich & Sridhar (1997).

The wave packet interaction time is $1/kV_A$, so that the relative change in velocity perturbation can be written as

$$\frac{\delta v_k}{v_k} \sim \frac{1}{v_k} \frac{dv_k}{dt} \frac{1}{kV_A} \sim \frac{v_k}{V_A},$$

where the time derivative is estimated from the nonlinear interaction term $\sim \mathbf{v} \cdot \nabla \mathbf{v} \sim kv_k^2$ of the MHD equations. Since $\delta v_k(t)$ is a random process with zero mean, it takes $N_k \sim (V_A/v_k)^2$ interactions before the velocity perturbations increase to $\sim v_k$. The time needed for that is $\tau_k = V_A/kv_k^2$. The energy flux across the spectrum is

$$\varepsilon \sim \frac{v_k^2}{\tau_k} \sim k \frac{v_k^4}{V_A}.$$

Assuming this flux to be constant in a steady state, we obtain the power spectrum of Alfvén waves

$$E_k^A \sim v_k^2/k \sim \frac{\sqrt{\varepsilon V_A}}{k^{3/2}}, \quad (\text{B9})$$

which is, of course, the I-K spectrum.

Now we need to relate the energy flux ε to its source in the acoustic turbulence of merging shocks. One possibility

is that three-wave interactions, such as decays of magnetoacoustic waves to other magnetoacoustic and Alfvén waves (Livshits & Tsytovich 1970; Kuznetsov 2001), $M \rightarrow M + A$ or $M \rightarrow A + A$, couple sufficiently broad ranges of the two spectra. On the other hand, the decay’s growth rate scales unfavorably with the wave number in the long wave limit, $\gamma_d \sim kV_A \delta B^2/B^2$, where the acoustic turbulence condensates. Besides, the weak turbulence scenario associated with the three-wave processes is not viable for a strong CR driver that seems to be present by virtue of the fit.

In strong turbulence regimes, the energy flux is usually obtained from a prescribed energy “injection” rate at an outer scale. In our case the Alfvén waves are fed in from a continuous acoustic spectrum rather than a determinate scale. However, the spectral shapes of these two spectra are formed by strong individual cascades without interaction, so they have markedly different indices (3 for acoustic- and 3/2 for Alfvén waves). Therefore, they must intersect, say at $k = k_*$ (cf. the Rhines scale). At this scale the turbulent kinetic energy of Alfvén waves is in equipartition with the acoustic energy (shocks), $E_{k_*}^A \sim E_{k_*}^s$. Since only one of them dominates for all k not too close to k_* , the interaction between them falls off with the growing $|k - k_*|$. The above equipartition requirement alone does not determine k_* and ε . The second condition that we need is that the energy transfer rates in the two cascades coincide at $k \sim k_*$. In the acoustic cascade this rate is the same as the shock coalescence rate, which is $\sim \gamma_D$ and is scale-invariant. Therefore, the second condition is $\varepsilon(k_*) \sim \gamma_D v_{k_*}^2$.

From these two conditions we find

$$k_* \sim \frac{\gamma_D}{V_A}, \quad \varepsilon \sim \gamma_D V_A^2, \quad (\text{B10})$$

that is $v_{k_*} \sim V_A$. In the range $k > k_*$ the two spectra separate from each other as follows

$$E_k^s \sim \frac{\gamma_D^2}{k^3}, \quad E_k^A \sim \frac{\sqrt{\gamma_D} V_A^{3/2}}{k^{3/2}}. \quad (\text{B11})$$

The behavior of the spectra at $k < k_*$ may deviate from these scalings, since the inverse acoustic cascade looses a significant part of its energy flux to the Alfvén forward cascade at $k \sim k_*$. In addition, the inverse Alfvén cascade may also proceed from k_* to smaller wave numbers at a different slope. Meanwhile, using the first of the two relations in Eq. (B10) we can express k_* through the “observable” quantity P_{CR} , which can be inferred from the fit,

$$k_* l_\perp \sim \frac{P_{\text{CR}}}{\rho C_s^2} \sqrt{\beta}. \quad (\text{B12})$$

Assuming that the background CR pressure is similar to the gas pressure, and it is enhanced by the reacceleration only by a factor of a few (according to the fit, $K = 2.4$, Sect. 5), the above ratio cannot be much larger than unity. Since for the highest energy reaccelerated CRs we assume $r_g \lesssim l_\perp$, the region $k < k_*$ is not important for the particle scattering. At the same time, the boundary in momentum space of self-confined particle at $r_g(p) \sim k_*^{-1}$ shifts to lower momenta

with growing P_{CR} , provided that l_{\perp} is constant. This shift limits the maximum energy of reaccelerated CRs that can be observed, unless there is a significant cascading of Alfvén waves to lower $k < k_*$.

C. ESTIMATE OF THE DISTANCE TO THE HYPOTHETICAL BOW-SHOCK

Now we can estimate the distance to the shock, ζ_{obs} , using an expression for the Alfvén wave spectrum in Eq. (B11). Since we use the nonlinearly transformed spectrum, the quasilinear phase integral in Eq. (A3) is no longer applicable and we turn to its original form in Eq. (6). We know the function of particle rigidity, $\Phi(R)$, on the l.h.s. of this equation from the fit while the particle diffusivity, κ_{int} , can be estimated as follows

$$\kappa_{\text{int}} \sim r_g c \frac{B^2}{\delta B_k^2} \sim r_g c \left. \frac{V_A^2}{v_k^2} \right|_{kr_g \sim 1}. \quad (\text{C13})$$

Introducing a dimensionless parameter, characterizing the CR pressure of reaccelerated particles,

$$\Pi = \frac{P_{\text{CR}}}{\rho C_s V_A},$$

so that $\gamma_D \sim \Pi V_A / l_{\perp}$, and using Eqs. (B9) with (B11), for κ_{int} we obtain

$$\kappa_{\text{int}} \sim \frac{c}{3} \sqrt{r_g l_{\perp} / \Pi}. \quad (\text{C14})$$

The base-line m.f.p. of reaccelerated particles propagating along the flux tube is thus

$$\lambda_{\text{CR}} \sim \sqrt{r_g l_{\perp}}.$$

Substituting $\kappa_{\parallel} = \kappa_{\text{int}}$ and $u_1 = \cos \vartheta_{nB} u$ in Eq. (6) and comparing it with Eq. (10), we may write

$$\sqrt{R_0} \simeq \frac{3u}{c \sqrt{r_{\text{GV}} l_{\perp}}} \Psi(\zeta_{\text{obs}}), \quad (\text{C15})$$

where

$$\Psi(\zeta) \equiv \int_0^{\zeta} \sqrt{\Pi} d\zeta,$$

and r_{GV} is the gyro-radius of a GV-proton. Note that, the rigidity R canceled out from the above relation and $R_0 \approx 4400$ can now be considered as a dimensionless number.

Next, we need to calculate the normalized CR pressure $\Pi(\zeta)$. Since it derives from the background CRs with a distribution f_{∞} , it is convenient to relate Π to the background CR pressure P_{∞} . From the solution of acceleration problem in Eq. (5) we have

$$\Pi = \frac{P_{\infty}}{\rho C_s V_A} \int_0^{\infty} R^3 (f - f_{\infty}) dR \Big/ \int_0^{\infty} f_{\infty} \frac{R^4 dR}{\sqrt{1 + R^2}}, \quad (\text{C16})$$

where the integral in the denominator represents the background CR pressure P_{∞} . The integration variable R is normalized here to the rest mass proton rigidity mc/e . In representing the pressure of reaccelerated CRs, characterized by

$f - f_{\infty}$, we have used the approximation $R \gg 1$. This approximation is not accurate near the shock, but as we have seen from crude estimates of ζ_{obs} in Sect. 3, the main contribution to the path integral comes from large ζ ahead of the shock precursor, where $f \approx f_{\infty}$ at $R \sim 1$. The main contribution to P_{∞} comes from $R \sim 1$, but the exact behavior of f_{∞} along the path is unknown (see however the discussion of the Voyager 1 data by Drury & Strong 2017). We attach this uncertainty to a new parameter $R_* \sim 1$, by assigning the lower limit of the integral in the denominator to R_* and replacing the square root expression by R .

The above expression for Π rewrites:

$$\Pi = \eta \int_0^{\infty} R^{3-\sigma} dR \exp \left[-\frac{\alpha}{\sqrt{R}} \Psi(\zeta_{\text{obs}}) \right], \quad (\text{C17})$$

where

$$\alpha = \frac{3u}{c \sqrt{r_{\text{GV}} l_{\perp}}} \quad \text{and} \quad \eta = \frac{K P_{\infty}}{\rho C_s V_A} \frac{\sigma - 4}{R_*^{4-\sigma}}. \quad (\text{C18})$$

Using Eq. (C17), we have the following differential equation for the path integral Ψ ,

$$\frac{d\Psi}{dz} = B \Psi^{4-\sigma},$$

where

$$B = \alpha^{4-\sigma} \sqrt{2\eta \Gamma(2\sigma - 8)},$$

and Γ is the gamma-function. After solving it and using Eq. (C15), we obtain the following result for ζ_{obs} :

$$\frac{\zeta_{\text{obs}}}{\sqrt{r_{\text{GV}} l_{\perp}}} = \frac{(c/3u) R_0^{(\sigma-3)/2} R_*^{2-\sigma/2} \sqrt{\rho C_s V_A}}{\sqrt{2(\sigma-4)} \sqrt{\Gamma(2\sigma-8)} (\sigma-3) \sqrt{K P_{\infty}}}. \quad (\text{C19})$$

By solving the last expression for R_0 , we obtain the result in Eq. (11).

D. LARGE- AND SMALL-SCALE ANISOTROPY

The purpose of this Appendix is to supplement Sect. 7 with further discussion of observations and interpretations of the CR anisotropy at different scales, as well as less essential details of the methods we used there.

Since the discovery of a narrow component in the CR arrival direction by Milagro observatory (Abdo et al. 2008), much have been learned about CRs in the same rigidity range 1–20 TV. Based on this learning, we have concluded Sect. 7 by linking together the recently detected rigidity bump with the sharp field-aligned CR excess, and the step-like increase in the CR intensity across the magnetic horizon. Note, that these two groups of particles are well separated in the cosine of pitch angle, μ , as they concentrate near $\mu = 1$ and $\mu = 0$, respectively. The “glue” for these three ingredients is the I-K turbulence spectrum required by the fit of the CR bump rigidity profile.

The I-K turbulence is also consistent with the step-like increase across the magnetic horizon. The effect of the turbulence spectrum on the sharp angular component, concentrated near $\mu = 1$, is weaker than that on the other two ingredients. The reason for that is the pitch angle dependence

of the scattering frequency that vanishes at $\mu = 1$ regardless of the scattering turbulence. The causally linked new observational findings give us a fresh glimpse of the Milagro hot spots, discovered more than a decade ago.

The Milagro sharp excess was found to be aligned with the heliotail direction, which is now believed to be not far from the local magnetic field direction (see, e.g., [Abeysekara et al. 2019](#) and Sect. 8). Though it is unlikely to be a heliotail phenomenon. Thanks to the combined action of the solar wind and the Sun’s motion through the ISM at $\approx 26 \text{ km s}^{-1}$, the heliosphere is a strongly elongated magnetic cavity ([Pogorelov et al. 2015](#)) with an average field being significantly lower inside than outside. Since the Larmor radius of a 10-TeV proton in a $1 \mu\text{G}$ field is $\approx 2000 \text{ au}$, while the heliosphere is only 200-300 au across and shrinks towards the tail, these particles cannot be *accelerated* there or even significantly deflected upon entrance. The field inside the cavity is just too weak, or its coherence length is too small, or both. If we still assume that a strong deflection somehow occurs, we will need to accept that the rigidity bump and the enhanced anisotropy in the same 1-10 TV range are not causally associated. Indeed, since the magnetic field at a local scale can be considered as static, it could not create the energy bump in the isotropic CR component, no matter how much of a CR deflection it might produce. It is therefore more likely that the anisotropy have been built up externally.

Several such mechanisms have been suggested and in part reviewed critically, e.g., by [Malkov \(2015\)](#), and more extensively by [Ahlers & Mertsch \(2017\)](#). Some of these mechanisms employ the CR propagation in a particular realization of the ISM turbulence (*not ensemble-averaged*). In principle, magnetic perturbations could produce a magnetic lensing effect, similar to the light ray caustics in refractive media. A simple example is a highly variable light pattern seen on the bottom of a swimming pool in a sunny day. However, such a particle focusing strongly depends on their rigidity. The 1 TV and 10 TV protons cannot be collimated simultaneously to produce the same hot spot in the sky, which, however, was observed by Milagro. In fact, they found that the spectrum of the collimated particles is flatter than the background. This behavior can hardly be consistent with the magnetic lensing effect, but suggests that the hot spot in the angular distribution and the rigidity bump are two sides of the same phenomenon.

An *ensemble-averaged*, and thereby more robust collimation mechanism, suggested by [Malkov et al. \(2010a\)](#), correctly predicts the Milagro sharp component’s parameters, including the spectral hardening between 1–10 TV. It assumes magnetic connectivity of the source and heliosphere, as is also proposed in the present paper, but the Milagro-related model *requires* the source to be at a few 100 pc, most likely being an SNR. The similarity with the mechanism described in Sect. 7 is in that the small scale anisotropy is also built on a larger-scale anisotropy, near its minimum at $\mu = 1$ of the first mode of the scattering operator, $f_1(\mu)$. One difference, however, is in that the CRs from the distant source are pitch-angle scattered on an anisotropic Goldreich-

Shridhar wave spectrum towards the minimum of $f_1(\mu)$ at $\mu = 1$. In the I-K turbulence, inferred earlier in this paper, the small scale anisotropy would be an addition of the second eigenfunction f_2 , to the larger-scale component f_1 . This composition requires a much closer source than any of the known SNRs, since the f_2 component would have decayed at such long distance.

Nevertheless, both in the nearby shock and SNR scenarios, the small scale anisotropy forms in the source’s loss-cone, that is at the minimum of $f_1(\mu)$. (Observe a decrease in f_1 at $\mu = \chi = 1$, in Fig. 6). The loss cone in momentum space develops at the dimensionless distance $\zeta \lesssim 1/\lambda_1$ from the source, because particles moving close to the magnetic axis are poorly scattered and escape along the field. So, apart from the almost isotropic f_0 , the f_1 component dominates the solution at $\zeta \gtrsim 1/\lambda_1$. In the range $1/\lambda_2 < \zeta < 1/\lambda_1$, both f_1 and f_2 may be visible, depending on the source angular profile. Adding them up we obtain a narrow excess in a broader deficit area on the intensity map, around the field direction. This appears to be consistent with the intensity map shown in Fig. 11 of [Abeysekara et al. \(2019\)](#). But should it always be?

Indeed, the minimum of f_1 is not necessarily the minimum on the overall intensity map. Evidently, f_1 and f_2 have a common isolated source, while the overall large-scale anisotropy is likely to originate from a stronger background CR component. It may have a minimum on the opposite side of the field line, for example. This is possible if the background CRs come from the Galactic center direction, which is roughly opposite to the heliotail. The background CR may also be formed by distributed CR sources, each of which having an individual loss cone, not seen at the heliosphere position for the reasons described above. Diamagnetic and curvature drifts in a possibly complicated magnetic environment around the heliosphere may further distort and mix up the CR background particles.

Although the above straightforward considerations speak for not to require the coincidence of the global intensity minimum with the sharp excess, it has been brought up as an issue by [Ahlers & Mertsch \(2017\)](#) in their discussion of the model of [Malkov et al. \(2010a\)](#). Note that this issue has already been addressed in Sect. 6 of this reference. More interestingly, as we noted, the intensity map in Fig. 11 presented by [Abeysekara et al. \(2019\)](#) can be interpreted as a narrow excess in a broad deficit near the point $-\mathbf{B}_{\text{IMF}}$ (relatively narrow red “island” surrounded by the blue “sea”). However, the slice through this map near longitude $\delta = -20^\circ$, shown in Fig. 8 of their paper, seems to be at a flat top of the intensity curve. It is also worth noting that a clear excess in the slice is seen in the HAWC, but not in the IceCube data set. Going back to the Milagro results, a possibly related sharp excess is between the minimum and the maximum, though closer to the latter. To make matters even more complicated, the deficit around an excess may also be a data processing effect ([Abdo et al. 2008](#)).

To conclude this discussion, the available small-scale anisotropy data are not sufficient to scrutinize the models

proposed in Malkov et al. (2010a) and in the present paper. At the same time, the sharp intensity growth across the magnetic equator is consistent with the effect of a nearby source combined with the I-K propagation regime. An interesting implication of this behavior is that there should be very little mirroring across the magnetic horizon. The turbulence should be largely incompressible at the relevant scales in the heliospheric environment. The present model also constrains the source distances required to observe both the intensity enhancement inside the loss-cone at $\mu = 1$ and the step-wise increase across the magnetic horizon at $\mu = 0$.

Turning to the details omitted in Sect. 7, the coefficients entering Eq. (20) are defined in a standard fashion:

$$C_n = \int_{-1}^1 \chi^3 Q_1(\chi) f_n(\chi) d\chi, \quad (\text{D20})$$

Here $\{f_n(\chi)\}_{n=0}^{\infty}$ is an orthonormal system of eigenfunctions obtained from the following spectral problem

$$\frac{\partial}{\partial \chi} (1 - \chi^4) \frac{\partial f}{\partial \chi} - \nu_{\perp} f = -\lambda \chi^3 f \quad (\text{D21})$$

with the inner product defined as follows

$$(f_n, f_m) \equiv \int_{-1}^1 f_n(\chi) f_m(\chi) \chi^3 d\chi = \delta_{nm},$$

while

$$\int_{-1}^1 f_n(-\chi) f_m(\chi) \chi^3 d\chi = 0$$

for all n and m .

This spectral problem is set by a condition of regularity of f_n at the singular points $\chi = \pm 1$ in Eq. (D21). No specific boundary condition is needed, which corresponds to the so-called Weyl's limit point case for this Sturm-Liouville problem. When obtaining the $\nu_{\perp} f$ term in Eq. (D21) by integrating across the flux tube from its axis to the boundary, we make a simple assumption $\nu_{\perp} = \text{const}$, even though it must depend on χ . The flux tube boundary is where the pitch angle scattering frequency D drops, as the particle self-driven turbulence drops beyond this point. Particles that cross this boundary are assumed to escape along the field line, so that the turbulence is not driven outside of the tube, as long as $\nu_{\perp} \ll 1$. A more realistic determination of this quantity is not worthwhile for our purpose, as it is likely to be small indeed, as we argued in Sect. 7. By virtue of the symmetry of Eq. (19), $f(-\zeta, \chi) = f(\zeta, -\chi)$ and the condition $\nu_{\perp} > 0$, the discrete spectrum is also symmetric and consists of an infinite sequence, $\pm\lambda_0, \pm\lambda_1, \pm\lambda_2, \dots$ of eigenvalues ordered as follows: $0 < \lambda_0 < \lambda_1 < \lambda_2, \dots$ (Richardson 1918). Our sign convention is that each $f_n(\chi)$ corresponds to $\lambda_n > 0$, while the negative eigenvalues $-\lambda_n$ correspond to $f_n(-\chi)$.

REFERENCES

- Abdo, A. A., Allen, B., Aune, T., et al. 2008, *Physical Review Letters*, 101, 221101, doi: [10.1103/PhysRevLett.101.221101](https://doi.org/10.1103/PhysRevLett.101.221101)
- Abeysekara, A., Alfaro, R., Alvarez, C., et al. 2019, *The Astrophysical Journal*, 871, 96
- Ackermann, M., Ajello, M., Albert, A., et al. 2014, *Phys. Rev. Lett.*, 112, 151103, doi: [10.1103/PhysRevLett.112.151103](https://doi.org/10.1103/PhysRevLett.112.151103)
- Adriani, O., Barbarino, G. C., Bazilevskaya, G. A., et al. 2011, *Science*, 332, 69, doi: [10.1126/science.1199172](https://doi.org/10.1126/science.1199172)
- Adriani, O., Akaike, Y., Asano, K., et al. 2019, *Phys. Rev. Lett.*, 122, 181102, doi: [10.1103/PhysRevLett.122.181102](https://doi.org/10.1103/PhysRevLett.122.181102)
- Aguilar, M., Aisa, D., Alpat, B., et al. 2015a, *Phys. Rev. Lett.*, 114, 171103, doi: [10.1103/PhysRevLett.114.171103](https://doi.org/10.1103/PhysRevLett.114.171103)
- . 2015b, *Phys. Rev. Lett.*, 115, 211101, doi: [10.1103/PhysRevLett.115.211101](https://doi.org/10.1103/PhysRevLett.115.211101)
- Aguilar, M., Ali Cavasonza, L., Alpat, B., et al. 2017, *Phys. Rev. Lett.*, 119, 251101, doi: [10.1103/PhysRevLett.119.251101](https://doi.org/10.1103/PhysRevLett.119.251101)
- Aguilar, M., Ali Cavasonza, L., Ambrosi, G., et al. 2018a, *Phys. Rev. Lett.*, 120, 021101, doi: [10.1103/PhysRevLett.120.021101](https://doi.org/10.1103/PhysRevLett.120.021101)
- Aguilar, M., Ali Cavasonza, L., Alpat, B., et al. 2018b, *Phys. Rev. Lett.*, 121, 051103, doi: [10.1103/PhysRevLett.121.051103](https://doi.org/10.1103/PhysRevLett.121.051103)
- Aguilar, M., Ali Cavasonza, L., Ambrosi, G., et al. 2020, *Phys. Rev. Lett.*, 124, 211102, doi: [10.1103/PhysRevLett.124.211102](https://doi.org/10.1103/PhysRevLett.124.211102)
- Aguilar, M., Cavasonza, L. A., Allen, M. S., et al. 2021, *Phys. Rev. Lett.*, 126, 041104, doi: [10.1103/PhysRevLett.126.041104](https://doi.org/10.1103/PhysRevLett.126.041104)
- Ahlers, M., & Mertsch, P. 2017, *Progress in Particle and Nuclear Physics*, 94, 184
- Ahn, H. S., Seo, E. S., Adams, J. H., et al. 2006, *Advances in Space Research*, 37, 1950, doi: [10.1016/j.asr.2005.09.031](https://doi.org/10.1016/j.asr.2005.09.031)
- Ahn, H. S., Allison, P. S., Bagliesi, M. G., et al. 2008, *Astroparticle Physics*, 30, 133, doi: [10.1016/j.astropartphys.2008.07.010](https://doi.org/10.1016/j.astropartphys.2008.07.010)
- Ahn, H. S., Allison, P., Bagliesi, M. G., et al. 2010, *Astrophys. J. Lett.*, 714, L89, doi: [10.1088/2041-8205/714/1/L89](https://doi.org/10.1088/2041-8205/714/1/L89)
- Aloisio, R., Blasi, P., & Serpico, P. D. 2015, *Astronomy and Astrophys.*, 583, A95, doi: [10.1051/0004-6361/201526877](https://doi.org/10.1051/0004-6361/201526877)
- Amenomori, M., Bi, X. J., Chen, D., et al. 2017, *Astrophys. J.*, 836, 153, doi: [10.3847/1538-4357/836/2/153](https://doi.org/10.3847/1538-4357/836/2/153)
- An, Q., Asfandiyarov, R., Azzarello, P., et al. 2019, *Science Adv.*, 5, doi: [10.1126/sciadv.aax3793](https://doi.org/10.1126/sciadv.aax3793)
- Atkin, E., Bulatov, V., Dorokhov, V., et al. 2018, *Soviet JETP Lett.*, 108, 5, doi: [10.1134/S0021364018130015](https://doi.org/10.1134/S0021364018130015)
- Atkin, E. V., Bulatov, V. L., Vasiliev, O. A., et al. 2019, *Astron. Reports*, 63, 66, doi: [10.1134/S1063772919010013](https://doi.org/10.1134/S1063772919010013)

- Axford, W. I. 1972, The Interaction of the Solar Wind With the Interstellar Medium. NASA Special Publication, ed. C. P. Sonett, P. J. Coleman, & J. M. Wilcox, Vol. 308, 609
- Baines, E. K., & Armstrong, J. T. 2012, *Astrophys. J.*, 744, 138, doi: [10.1088/0004-637X/744/2/138](https://doi.org/10.1088/0004-637X/744/2/138)
- Bell, A. R. 1978, *Mon. Not. R. Astron. Soc.*, 182, 147
- . 2004, *Mon. Not. R. Astron. Soc.*, 353, 550, doi: [10.1111/j.1365-2966.2004.08097.x](https://doi.org/10.1111/j.1365-2966.2004.08097.x)
- Berghöfer, T. W., & Breitschwerdt, D. 2002, *Astronomy and Astrophys.*, 390, 299, doi: [10.1051/0004-6361:20020627](https://doi.org/10.1051/0004-6361:20020627)
- Binns, W. R., Israel, M. H., Christian, E. R., et al. 2016, *Science*, 352, 677, doi: [10.1126/science.aad6004](https://doi.org/10.1126/science.aad6004)
- Blandford, R. D., & Ostriker, J. P. 1978, *Astrophys. J. Lett.*, 221, L29, doi: [10.1086/182658](https://doi.org/10.1086/182658)
- Blasi, P., Amato, E., & Serpico, P. D. 2012, *Phys. Rev. Lett.*, 109, 061101, doi: [10.1103/PhysRevLett.109.061101](https://doi.org/10.1103/PhysRevLett.109.061101)
- Boschini, M. J., Della Torre, S., Gervasi, M., et al. 2020a, *Astrophys. J.*, 889, 167, doi: [10.3847/1538-4357/ab64f1](https://doi.org/10.3847/1538-4357/ab64f1)
- . 2020b, *Astrophys. J. Suppl.*, 250, 27, doi: [10.3847/1538-4365/aba901](https://doi.org/10.3847/1538-4365/aba901)
- . 2021, arXiv e-prints, arXiv:2101.12735. <https://arxiv.org/abs/2101.12735>
- Breitschwerdt, D., Feige, J., Schulreich, M. M., et al. 2016, *Nature*, 532, 73, doi: [10.1038/nature17424](https://doi.org/10.1038/nature17424)
- Breitschwerdt, D., & Schmutzler, T. 1999, *Astronomy and Astrophys.*, 347, 650. <https://arxiv.org/abs/astro-ph/9902268>
- Burgasser, A. J., Gillon, M., Melis, C., et al. 2015, The Astronomical Journal, 149, 104, doi: [10.1088/0004-6256/149/3/104](https://doi.org/10.1088/0004-6256/149/3/104)
- Bykov, A., Petrov, A., Krassilchchikov, A., et al. 2019, The Astrophysical Journal Letters, 876, L8
- Cook, D. L., Berger, E., Faestermann, T., et al. 2009, in *Lunar and Planetary Science Conf.*, 1129
- Cowsik, R., & Madziwa-Nussinov, T. 2016, The Astrophysical Journal, 827, 119
- Cox, D. P., & Helenius, L. 2003, The Astrophysical Journal, 583, 205, doi: [10.1086/344926](https://doi.org/10.1086/344926)
- Crawford, I., Lalllement, R., & Welsh, B. 1998, Monthly Notices of the Royal Astronomical Society, 300, 1181
- Cummings, A. C., Stone, E. C., Heikkilä, B. C., et al. 2016, *Astrophys. J.*, 831, 18, doi: [10.3847/0004-637X/831/1/18](https://doi.org/10.3847/0004-637X/831/1/18)
- D'Arrest, M. 1847, *Mon. Not. R. Astron. Soc.*, 8, 16, doi: [10.1093/mnras/8.1.16](https://doi.org/10.1093/mnras/8.1.16)
- de Wit, T. D., Krasnoselskikh, V. V., Bale, S. D., et al. 2020, The Astrophysical Journal Supplement Series, 246, 39
- Dehnen, W. 1999, The Astrophysical Journal, 524, L35, doi: [10.1086/312299](https://doi.org/10.1086/312299)
- Dieterich, S. B., Weinberger, A. J., Boss, A. P., et al. 2018, *Astrophys. J.*, 865, 28, doi: [10.3847/1538-4357/aadadc](https://doi.org/10.3847/1538-4357/aadadc)
- Dorfi, E. 1984, Advances in Space Research, 4, 205, doi: [10.1016/0273-1177\(84\)90313-2](https://doi.org/10.1016/0273-1177(84)90313-2)
- Drury, L. O. 1983, Reports on Progress in Physics, 46, 973
- Drury, L. O. C., & Falle, S. A. E. G. 1986, *Mon. Not. R. Astron. Soc.*, 223, 353
- Drury, L. O. C., & Strong, A. W. 2017, *Astronomy and Astrophys.*, 597, A117, doi: [10.1051/0004-6361/201629526](https://doi.org/10.1051/0004-6361/201629526)
- Dupuy, T. J., Liu, M. C., Best, W. M. J., et al. 2019, *AJ*, 158, 174, doi: [10.3847/1538-3881/ab3cd1](https://doi.org/10.3847/1538-3881/ab3cd1)
- Fang, K., Bi, X.-J., & Yin, P.-F. 2020, arXiv e-prints, arXiv:2003.13635. <https://arxiv.org/abs/2003.13635>
- Ferrière, K. 2015, in Journal of Physics: Conference Series, Vol. 577, 012008
- Fimiani, L., Cook, D. L., Faestermann, T., et al. 2012, in *Lunar and Planetary Science Conf.*, 1279
- Fimiani, L., Cook, D. L., Faestermann, T., et al. 2014, in *Lunar and Planetary Science Conf.*, 1778
- Fornieri, O., Gaggero, D., Guberman, D., Brahimi, L., & Marcowith, A. 2020, arXiv e-prints, arXiv:2007.15321. <https://arxiv.org/abs/2007.15321>
- Frisch, P., Berdyugin, A., Piirola, V., et al. 2015, The Astrophysical Journal, 814, 112
- Frisch, P. C., Redfield, S., & Slavin, J. D. 2011, *Ann. Rev. Astron. Astroph.*, 49, 237, doi: [10.1146/annurev-astro-081710-102613](https://doi.org/10.1146/annurev-astro-081710-102613)
- Fry, B. J., Fields, B. D., & Ellis, J. R. 2015, *Astrophys. J.*, 800, 71, doi: [10.1088/0004-637X/800/1/71](https://doi.org/10.1088/0004-637X/800/1/71)
- Furno, I., Intrator, T., Ryutov, D., et al. 2006, Physical review letters, 97, 015002
- Giacinti, G., Kachelrieß, M., & Semikoz, D. V. 2018, *J. Cosmol. and Astroparticle Phys.*, 2018, 051, doi: [10.1088/1475-7516/2018/07/051](https://doi.org/10.1088/1475-7516/2018/07/051)
- Goldreich, P., & Sridhar, S. 1997, *Astrophys. J.*, 485, 680, doi: [10.1086/304442](https://doi.org/10.1086/304442)
- Grebenyuk, V., Karmanov, D., Kovalev, I., et al. 2019a, *Adv. Spa. Res.*, 64, 2546, doi: [10.1016/j.asr.2019.10.004](https://doi.org/10.1016/j.asr.2019.10.004)
- . 2019b, *Adv. Spa. Res.*, 64, 2559, doi: [10.1016/j.asr.2019.06.030](https://doi.org/10.1016/j.asr.2019.06.030)
- Gry, C., & Jenkins, E. B. 2014, *Astronomy and Astrophys.*, 567, A58, doi: [10.1051/0004-6361/201323342](https://doi.org/10.1051/0004-6361/201323342)
- . 2017, *Astronomy and Astrophys.*, 598, A31, doi: [10.1051/0004-6361/201628987](https://doi.org/10.1051/0004-6361/201628987)
- Hanusch, A., Liseykina, T. V., & Malkov, M. 2019, *Astrophys. J.*, 872, 108, doi: [10.3847/1538-4357/aafdae](https://doi.org/10.3847/1538-4357/aafdae)
- Haverkorn, M., Brown, J., Gaensler, B., & McClure-Griffiths, N. 2008, The Astrophysical Journal, 680, 362
- Kang, H., Jones, T. W., & Ryu, D. 1992, *Astrophys. J.*, 385, 193, doi: [10.1086/170927](https://doi.org/10.1086/170927)
- Kennel, C. F. 1988, Journal of Geophysical Research: Space Physics, 93, 8545, doi: [10.1029/JA093iA08p08545](https://doi.org/10.1029/JA093iA08p08545)

- Knie, K., Korschinek, G., Faestermann, T., et al. 2004, *Phys. Rev. Lett.*, 93, 171103, doi: [10.1103/PhysRevLett.93.171103](https://doi.org/10.1103/PhysRevLett.93.171103)
- . 1999, *Phys. Rev. Lett.*, 83, 18, doi: [10.1103/PhysRevLett.83.18](https://doi.org/10.1103/PhysRevLett.83.18)
- Koll, D., Korschinek, G., Faestermann, T., et al. 2019, *Phys. Rev. Lett.*, 123, 072701, doi: [10.1103/PhysRevLett.123.072701](https://doi.org/10.1103/PhysRevLett.123.072701)
- Kulsrud, R., & Pearce, W. P. 1969, *Astrophys. J.*, 156, 445, doi: [10.1086/149981](https://doi.org/10.1086/149981)
- Kuznetsov, E. A. 2001, *Journal of Experimental & Theoretical Physics*, 93, 1052, <https://link.springer.com/article/10.1134/1.1427116>
- Lallement, R., Quémerais, E., Bertaux, J.-L., et al. 2005, *Science*, 307, 1447
- Landau, L. D., & Lifshitz, E. M. 1987, *Fluid Mechanics* (Pergamon Press)
- Linsky, J. L., Redfield, S., & Tilipman, D. 2019, *Astrophys. J.*, 886, 41, doi: [10.3847/1538-4357/ab498a](https://doi.org/10.3847/1538-4357/ab498a)
- Lipari, P., & Vernetto, S. 2020, *Astropart. Phys.*, 120, 102441, doi: [10.1016/j.astropartphys.2020.102441](https://doi.org/10.1016/j.astropartphys.2020.102441)
- Livshits, M., & Tsytovich, V. 1970, *Nuclear Fusion*, 10, 241, doi: [10.1088/0029-5515/10/3/003](https://doi.org/10.1088/0029-5515/10/3/003)
- Ludwig, P., Bishop, S., Egli, R., et al. 2016, *Proc. of NAS*, 113, 9232, doi: [10.1073/pnas.1601040113](https://doi.org/10.1073/pnas.1601040113)
- Luthardt, L., & Roessler, R. 2017, *Geology*, 45, 279
- Lutomirski, R. F., & Sudan, R. N. 1966, *Physical Review*, 147, 156, doi: [10.1103/PhysRev.147.156](https://doi.org/10.1103/PhysRev.147.156)
- Malkov, M. A. 1998, *Phys. Rev. E*, 58, 4911
- . 2015, *Physics of Plasmas*, 22, 091505, doi: [10.1063/1.4928941](https://doi.org/10.1063/1.4928941)
- Malkov, M. A., & Aharonian, F. A. 2019, *Astrophys. J.*, 881, 2, doi: [10.3847/1538-4357/ab2c01](https://doi.org/10.3847/1538-4357/ab2c01)
- Malkov, M. A., & Diamond, P. H. 2009, *Astrophys. J.*, 692, 1571, doi: [10.1088/0004-637X/692/2/1571](https://doi.org/10.1088/0004-637X/692/2/1571)
- Malkov, M. A., Diamond, P. H., O'C. Drury, L., & Sagdeev, R. Z. 2010a, *Astrophys. J.*, 721, 750, doi: [10.1088/0004-637X/721/1/750](https://doi.org/10.1088/0004-637X/721/1/750)
- Malkov, M. A., Diamond, P. H., & Sagdeev, R. Z. 2010b, *Plasma Physics and Controlled Fusion*, 52, 124006, doi: [10.1088/0741-3335/52/12/124006](https://doi.org/10.1088/0741-3335/52/12/124006)
- Mamajek, E. E., Barenfeld, S. A., Ivanov, V. D., et al. 2015, *Astrophys. J. Lett.*, 800, L17, doi: [10.1088/2041-8205/800/1/L17](https://doi.org/10.1088/2041-8205/800/1/L17)
- McKenzie, J. F., & Voelk, H. J. 1982, *Astronomy and Astrophys.*, 116, 191
- Niu, J.-S. 2020, arXiv e-prints, arXiv:2009.00884, <https://arxiv.org/abs/2009.00884>
- Panov, A. D., Adams, J. H., Ahn, H. S., et al. 2009, *Bull. Russian Acad. Sci., Physics*, 73, 564, doi: [10.3103/S1062873809050098](https://doi.org/10.3103/S1062873809050098)
- Pogorelov, N. V., Borovikov, S. N., Heerikhuisen, J., & Zhang, M. 2015, *Astrophys. J. Lett.*, 812, L6, doi: [10.1088/2041-8205/812/1/L6](https://doi.org/10.1088/2041-8205/812/1/L6)
- Pouquet, A., Frisch, U., & Leorat, J. 1976, *Journal of Fluid Mechanics*, 77, 321, doi: [10.1017/S0022112076002140](https://doi.org/10.1017/S0022112076002140)
- Pouquet, A., Rosenberg, D., Stawarz, J. E., & Marino, R. 2018, *Helicity dynamics, inverse and bi-directional cascades in fluid and MHD turbulence: A brief review.* <https://arxiv.org/abs/1807.03239>
- Redfield, S., & Linsky, J. L. 2008, *Astrophys. J.*, 673, 283, doi: [10.1086/524002](https://doi.org/10.1086/524002)
- Rhines, P. B. 1975, *Journal of Fluid Mechanics*, 69, 417, doi: [10.1017/S0022112075001504](https://doi.org/10.1017/S0022112075001504)
- Richardson, R. G. D. 1918, *American Journal of Mathematics*, 40, 283. <http://www.jstor.org/stable/2370485>
- Rugel, G., Faestermann, T., Knie, K., et al. 2009, *Phys. Rev. Lett.*, 103, 072502, doi: [10.1103/PhysRevLett.103.072502](https://doi.org/10.1103/PhysRevLett.103.072502)
- Ryutov, D., Furno, I., Intrator, T., Abbate, S., & Madziwa-Nussinov, T. 2006, *Physics of plasmas*, 13, 032105
- Sagdeev, R. Z. 1966, *Reviews of Plasma Physics*, 4, 23
- Scholz, R. D. 2014, *Astronomy and Astrophys.*, 561, A113, doi: [10.1051/0004-6361/201323015](https://doi.org/10.1051/0004-6361/201323015)
- Sfeir, D. M., Lallement, R., Crifo, F., & Welsh, B. Y. 1999, *Astronomy and Astrophys.*, 346, 785
- Skilling, J. 1975, *Mon. Not. R. Astron. Soc.*, 172, 557
- Snowden, S. L., Chiao, M., Collier, M. R., et al. 2014, *Astrophys. J. Lett.*, 791, L14, doi: [10.1088/2041-8205/791/L14](https://doi.org/10.1088/2041-8205/791/L14)
- Spangler, S. R. 2009, *Plasma Turbulence in the Local Bubble*, ed. J. L. Linsky, V. V. Izmodenov, E. Möbius, & R. von Steiger (New York, NY: Springer New York), 277–290, doi: [10.1007/978-1-4419-0247-4_22](https://doi.org/10.1007/978-1-4419-0247-4_22)
- Strong, A. W., & Moskalenko, I. V. 1998, *The Astrophysical Journal*, 509, 212, doi: [10.1086/306470](https://doi.org/10.1086/306470)
- Vidal, M., Dickinson, C., Davies, R. D., & Leahy, J. P. 2015, *Mon. Not. R. Astron. Soc.*, 452, 656, doi: [10.1093/mnras/stv1328](https://doi.org/10.1093/mnras/stv1328)
- Vladimirov, A. E., Jóhannesson, G., Moskalenko, I. V., & Porter, T. A. 2012, *Astrophys. J.*, 752, 68, doi: [10.1088/0004-637X/752/1/68](https://doi.org/10.1088/0004-637X/752/1/68)
- Völk, H. J., Drury, L. O., & McKenzie, J. F. 1984, *Astronomy and Astrophys.*, 130, 19
- Wallner, A., Feige, J., Kinoshita, N., et al. 2016, *Nature*, 532, 69, doi: [10.1038/nature17196](https://doi.org/10.1038/nature17196)
- Whitham, G. B. 2011, *Linear and nonlinear waves*, Vol. 42 (John Wiley & Sons)
- Wiedenbeck, M. E., Binns, W. R., Christian, E. R., et al. 1999, *Astrophys. J. Lett.*, 523, L61, doi: [10.1086/312242](https://doi.org/10.1086/312242)
- Wood, B. E., Müller, H.-R., Zank, G. P., & Linsky, J. L. 2002, *The Astrophysical Journal*, 574, 412
- Yoon, Y. S., Ahn, H. S., Allison, P. S., et al. 2011, *Astrophys. J.*, 728, 122, doi: [10.1088/0004-637X/728/2/122](https://doi.org/10.1088/0004-637X/728/2/122)
- Yuan, Q., Qiao, B.-Q., Guo, Y.-Q., Fan, Y.-Z., & Bi, X.-J. 2020, arXiv e-prints, arXiv:2007.01768, <https://arxiv.org/abs/2007.01768>

Zirnstien, E., Heerikhuisen, J., Funsten, H., et al. 2016, The
Astrophysical Journal Letters, 818, L18